CHALMERS

PdAu Alloy Nanoparticles for Hydrogen Sensing

Master's Thesis

EMIL LIDSTRÖM

Department of Applied Physics
Division of Chemical Physics
CHALMERS UNIVERSITY OF TECHNOLOGY
Göteborg, Sweden 2014
Master's Thesis 2014

MASTER'S THESIS

PdAu Alloy Nanoparticles for Hydrogen Sensing

Emil Lidström

EXAMINER

Christoph Langhammer, Assistant Professor

SUPERVISOR

Carl Wadell, Licentiate of Engineering

Department of Applied Physics

Chemical Physics

CHALMERS UNIVERSITY OF TECHNOLOGY

Göteborg, Sweden 2014

PdAu Alloy Nanoparticles for Hydrogen Sensing

Master's Thesis within the Applied Physics Masters Programme
EMIL LIDSTRÖM

COVER
Left: Tilted SEM image of disk-shaped PdAu nanoparticles.
Right: Hydrogen ab-/desorption isotherm for PdAu nanoparticles (18 at% Au).

Abstract

The potential of a hydrogen economy introduces the need for efficient hydrogen storage as well as reliable gas sensors. Hydride-forming metal particles may be the solution to both these problems.

In this thesis we present a means of fabrication of PdAu alloy nanoparticles, suitable for LSPR sensing of hydrogen gas concentrations. Heterogeneous particles of stacked Pd+Au layers were fabricated using Hole-Mask Colloidal Lithography. The particles were annealed at different temperatures in order to promote alloying. Full alloying seems to be achieved at $500\,^{\circ}\mathrm{C}$, as was confirmed by XPS measurements and by hydrogen uptake characteristics.

Hydrogen ab-/desorption cycles were measured by monitoring the LSPR spectra of the particles while varying the hydrogen pressure. The hysteresis of the α-β transition decreased with increasing gold content, in agreement with measurements on thin films. The hydrogen ab-/desorption kinetics were faster for PdAu than for pure Pd particles and the rate limiting steps seem to be different.

Addition of Au may improve optical hydrogen sensors based on Pd. Nanoparticles may prove beneficial over thin films due to the possibility of LSPR sensing and faster kinetics due to shorter diffusion.

Contents

1

Introduction

1.1   Context

This thesis project was performed at a group with a wide interest in nanoplasmonics and, more recently, in metal hydride formation in nanomaterials. In the past, the group has been studying hydrogen storage in single-metal nanoparticles [1, 18], mainly with pure palladium as a model system. There is now an ambition to move towards more complex systems, mainly alloy materials, as this opens the door to systems better suitable for sensing and large-scale storage of hydrogen. As a first step in this direction, the fabrication of PdAu alloy nanoparticles is studied.

Nanostructuring of metals has been shown to improve hydrogen uptake properties [7]. A synergy thus arises from the fact that metal nanoparticles exhibit interesting optical properties, a subject of particular interest in the research group.

In addition to being a model system for the fabrication of alloys suitable for hydrogen storage, the PdAu nanoparticles presented in this thesis might have a direct application in the form of a hydrogen gas sensor.

Optical hydrogen sensors utilizing the hydrogen absorption of Pd are commercially available [23]. Several sensors using a PdAu alloy instead have been studied [21, 27]. The addition of gold is expected to improve the sensor in some regards, such as accuracy and stability. Using nanoparticles as opposed to thin films may be advantageous due to the plasmonic behaviour of nanoparticles. This enables sensing of a wavelength rather than an intensity, decreasing problems associated with intensity-shifts due to contamination. Nanostructuring might also lead to faster response due to shorter diffusion distances.

Many ways of fabricating PdAu alloys, both films [21, 31] and particles [26], have previously been studied. However, no example of alloying by annealing two stacked single-metal disks has been found in the literature. This thesis will thus contribute by presenting such a fabrication method and by adding knowledge about the PdAu system in nanostructures.

1.2 Aim

The main aim of the project was to find a way of producing PdAu alloy nanoparticles using methods available to the research group. These methods include the clean room tools used for Hole-Mask Colloidal Lithography (see section 3.1.1), single metal deposition through evaporation and annealing in a gas reactor.

The particles should be characterised in order to verify the alloying and to evaluate the obtained material. The structure, geometry, composition and homo-/heterogeneity of the samples were to be analysed. Some hydrogen absorption/desorption isotherms should be measured using plasmonic sensing in order to evaluate the sensing properties. The aim was to find a fabrication scheme for a sensor with a strong signal with an unambiguous relation to the hydrogen pressure.

An additional aim was to analyse the selectivity of the sensor (the signal for H_2 vs other gases, e.g. CO). In the end, no measurements were performed on this matter as other aspects of the system were given higher priority.

Originally, the plan was to also develop a fabrication technique for MgNi alloys, similar to the one used for PdAu. However, no tool was available for the deposition of magnesium and this part was abandoned in favour of more analysis of the PdAu system.

1.3 Scope

The nature of this thesis is mainly experimental. Some theory is presented in order to understand the subject and some qualitative theories are presented as interpretations of the results. The experiments evaluate the hydrogen uptake properties from a "sensing" point of view, measuring the change of the optical spectrum upon exposure to hydrogen. The actual amount of absorbed hydrogen has not been directly measured. However, the main signal that was measured is expected to be proportional to the hydrogen concentration inside the metal. Apart from the plasmonic measurements, XPS and SEM analysis have been used in order to verify the geometry and homogeneity of the particles.

The thesis presents results for disk-shaped PdAu nanoparticles fabricated by hole-mask colloidal lithography (including single-metal deposition) and annealing. The hydrogen uptake measurements have all been performed in an $Ar+H_2$ environment, the influence of other gases was not addressed. The cycling stability has been evaluated for up to ≈ 50 cycles. Long-term aging has not been addressed.

1.4 Research questions

Some of the central questions in this thesis are:

- Is it possible to fabricate PdAu alloy particles using the tools at hand, i.e. single-metal deposition and annealing? Can they be made homogeneous?

- How are the plasmonic, hydrogenation and sensing characteristics of such nanoparticles? Can the hysteresis in the isotherm be eliminated?

- How does gold content and annealing affect the sensing characteristics? Is there an optimal fabrication scheme?

- Do the characteristics of the nanoparticles differ from those of similar thin-film sensors?

2

Background

2.1 Hydrogen Fuel

4 kg of hydrogen is enough to travel 400 km in a car equipped with a state-of-the-art fuel cell and an electric motor [2]. Hydrogen is an extremely abundant element and the only product of its combustion is water. As pollution, climate change and "peak oil" are increasing concerns hydrogen is seen as a promising alternative, alongside electrochemical energy stored in batteries.

Today hydrogen is mainly produced from fossil fuels. During this production CO_2 is released, today hydrogen can thus not be seen as completely CO_2 neutral. Research is ongoing with the aim of producing hydrogen gas directly from water using sunlight [3]. Hydrogen can also be produced through electrolysis of water. This provides a way of creating a storable and transportable fuel from renewable, but intermittent, electric energy sources such as solar and wind power [13]. Apart from being used as a fuel, hydrogen gas is today present as a reactant in some chemical processes, such as methanol production [4].

Some limited production cars running on hydrogen already exist. The *Honda FCX Clarity* (seen in figure 2.1) uses a fuel cell and an electric motor [8]. The *BMW Hydrogen 7* can run on both gasoline and hydrogen using an internal combustion engine [9], perhaps demonstrating a smoother transition from fossil fuel to hydrogen.

Intense research is ongoing in the fields of hydrogen production and fuel cells [5]. However, if hydrogen is going to be used as a fuel, the issue of storing the hydrogen in a safe and efficient way needs to be dealt with as well.

2.1.1 Hydrogen Storage

Many ways of storing hydrogen have been proposed [2]. By "conventional storage" one usually refers to high pressure gas tanks. There are two main disadvantages of this technology: the low density and the risks associated with failure during compression or

4

Figure 2.1: The Honda FCX Clarity is a limited production car running on Hydrogen, using a fuel cell and an electric motor. From [10].

storage. Using liquid hydrogen significantly lowers the volume of the container. However, to protect from overpressure liquid hydrogen containers are open systems, leading to evaporation and loss of hydrogen as the container is heated by the environment.

Some metals bind chemically with hydrogen, forming so-called metal hydrides [6]. This may provide storage in lower volumes than both gas tanks and liquid hydrogen [2]. It also partly eliminates the risk of explosion as the hydrogen is not available in gas-form. Most metal hydrides suffer from problems such as high release temperatures, slow kinetics or unreasonably low gravimetric density of hydrogen ($\frac{m_{hydrogen}}{m_{metal-hydride}}$) [2, 7]. Some of these problems can be reduced by using the material in micro or nano structures [7].

The US Department of Energy has released a series of targets for storage in light-duty vehicles. These include gravimetric capacity ($7.5\,\text{wt}\%$), volumetric capacity ($0.07\,\text{kgH}_2/\text{L}$), maximum delivery temperature ($85\,^\circ\text{C}$) and fill time ($2.5\,\text{min}$) [11].

2.1.2 Risks and Need for Hydrogen Sensing

An issue often mentioned when speaking of hydrogen-powered vehicles is the explosion risk, particularly the example of the Hindenburg Catastrophe tends to be brought up. However, recent analysis claims that the airship caught fire due to the highly flammable skin material rather than the hydrogen [2]. Use of hydrogen fuel does also not seem to decrease the safety when used in road vehicles, compared to the usage of gasoline [12].

Although it might not be more dangerous than gasoline, there are certainly risks involved in the use of hydrogen. Hydrogen is highly flammable due to low ignition temperature, high heat of combustion and a wide flammable range (4-75%). The small molecular size of hydrogen makes leakage a problem at all stages of usage (production, storage, transportation, etc.). Hydrogen refilling of high pressure gas tanks involves particularly high risks [2, 13]. Cheap, reliable and safe (non-spark-producing) hydrogen

gas sensors are thus of increasing interest. Also here metal hydrides may play a crucial part.

2.2 Metal Hydrides

Many metals bond chemically with hydrogen. This can be used as a means of storage by pumping hydrogen into the metal and later releasing it by altering the pressure and possibly also the temperature.

When a hydride forming metal is exposed to an increasing external hydrogen pressure, the concentration typically changes according to figure 2.2. Initially, the hydrogen exists in the so-called α-phase [18]. The H-H interaction is negligible and the H atoms behave as a gas inside the metal. In this phase Sieverts law is valid:

$$\sqrt{P_{H_2}} = C_H \cdot K_{Sieverts} \tag{2.1}$$

where P_{H_2} is the external hydrogen pressure, C_H the hydrogen concentration inside the metal and $K_{Sieverts}$ is the Sieverts constant. As is seen in figure 2.2, the behaviour varies significantly with temperature, as does the value of $K_{Sieverts}$. The enthalpy of formation of the α-phase (i.e. enthalpy of solution) can be found by plotting the $K_{Sieverts}$ vs T^{-1} and finding the slope, see left-hand side of figure 2.2.

At higher concentrations the H-H interaction has more influence. As the interaction is attractive the hydrogen atoms form cluters, nuclei of a new phase, that grow with increasing pressure until they become thermodynamically stable, this is called the β-phase (right-hand side of isotherm in figure 2.2). The transition from the α- to the β-phase ideally occurs at a constant pressure $P_{\alpha\beta}$ and is of first order. Above the critical temperature T_c the transition is continuous, for pure bulk Pd this temperature is 298 °C [18]. Thermodynamic parameters of the β-phase can be found in a so-called *Van't Hoff plot*, showing the plateau pressure P_{H_2} vs $1/T$ (see the right-hand side of figure 2.2).

2.3 Plasmons and LSPR sensing

Light interacts in interesting ways with nano-sized metal particles. Many applications of this have been presented [17, 19] and perhaps the most promising applications are in sensing and measurements. The main reference for this chapter is the doctoral thesis of *C. Langhammer* [18].

Plasmons are excitations in the oscillation of the free electron gas [18]. Due to the frequency dependence of the dielectric function, metals transmit light of different wavelength/colour differently. The frequency dependence changes if the metal is in the form of a nano particle rather than a bulk.

In metal particles of the size to be studied the whole free electron gas can be collectively excited. Simplified, this can be pictured as the metal and its free electron gas behaving as a spring (as pictured in figure 2.3). The electric field induces a charge separation, the electron gas is slightly dislocated from the positive nuclei. This separation
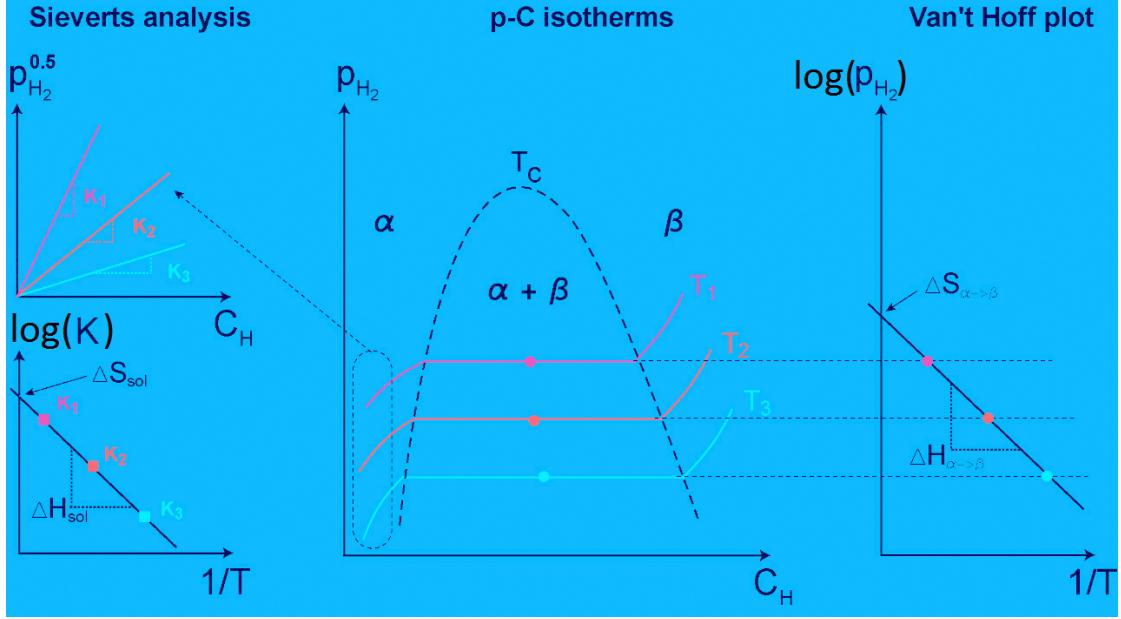
Figure 2.2: Typical isotherms for the formation of metal hydrides. The hydrogen initially exists in the α-phase where the hydrogen concentration is low enough for the H-H interaction to be negligible. The enthalpy of formation of the α-phase can be found from the shape of the isotherm according to the Sieverts analysis. The transition to the β-phase occurs at a constant plateau pressure. By plotting the temperature dependence of this pressure one can find the enthalpy of formation of the β-phase. Figure modified from *Christoph Langhammer*.

causes a restoring force between the electrons and the nuclei, similar to a classical spring. This excitation is called an LSPR, localised surface plasmon resonance, and provides a useful experimental tool. If light is sent through a sample covered in metal nanoparticles some of the photons will excite plasmons. This will lead to either scattering or absorption of the light, both yielding an extinction in the spectrum of the outgoing light. The LSPR frequency can then be seen as a peak in this extinction spectrum.

An introduction to the modelling of plasmons is given in [18]. To be brief, one can estimate the frequency-dependence of the extinction by assuming a spherical particle. For a particle with a diameter $D << \lambda$, the polarizability is given by

$$\alpha(\omega) \approx 4\pi \left(\frac{D}{2} \right)^3 \cdot \frac{\epsilon(\omega)_m - \epsilon_d}{\epsilon(\omega)_m + 2\epsilon_d} \tag{2.2}$$

where $\epsilon(\omega)_m$ is the complex dielectric function of the metal and ϵ_d the dielectric constant of the surrounding medium. The complex dielectric function of a metal can be estimated by using a free electron model (Drude electrons). The polarizability can then be written in the form

$$\alpha(\omega) \approx 4\pi \left(\frac{D}{2} \right)^3 \cdot \frac{\omega^2{}_{LSPR}}{\omega^2{}_{LSPR} - \omega^2 - i\Gamma\omega} \tag{2.3}$$
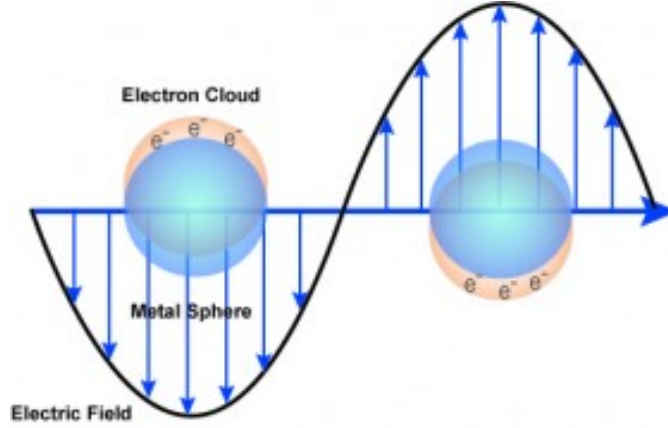
Figure 2.3: The localised surface plasmon resonance can be pictured as a spring (the free electrons) oscillating in resonance with light of a certain frequency. The light causes a charge separation, displacing the electron gas from the positive nuclei. The restoring spring force is provided by the electric field created by this displacement. With permission from *nanoComposix* [20].

where the resonance frequency ω_{LSPR} is related to the plasma frequency ω_P of the metal according to $\omega_{LSPR} = \frac{\omega_P}{\sqrt{1-2\epsilon_d}}$. The extinction cross section is then given by the expression

$$\sigma_{extinction} = k \cdot \text{Im}(\alpha\omega) \tag{2.4}$$

where k is the wave number of the incident light. This frequency dependence will change as the particle shape deviates from the sphere. One may approximate a disk as an oblate spheroid ("M&M-shape"). In this case the frequency dependence will change with the eccentricity $e = \sqrt{1 - \frac{D^2}{h^2}}$, where D and h are the diameter and the height of the disk. For a given metal, the LSPR-peak can thus be tuned for a certain sensing application by altering the height or diameter of the particles.

The LSPR peak shifts upon some chemical or physical changes of the particle or its surroundings. We can understand this from equation (2.2), ϵ_d may change if different substances are added to the surrounding of the particle and $\epsilon(\omega)_m$ may change if the particle itself is altered (e.g. it absorbs hydrogen). A measurement can thus be performed, as in figure 2.4, by sending light through a sample and recording the spectrum of the outgoing light. By comparing this with the incoming light the wavelength λ of the extinction peak can be found. By altering the environment of the nanoparticles (e.g. exposing it to hydrogen) and recording the shift of this peak $\Delta\lambda$ the physical or chemical process of interest may be studied.

2.4 Hydrogen Sensors

As mentioned before, mass usage of hydrogen introduces the risk of explosions due to leakage. This may increase the interest for hydrogen sensors. Plausible applications
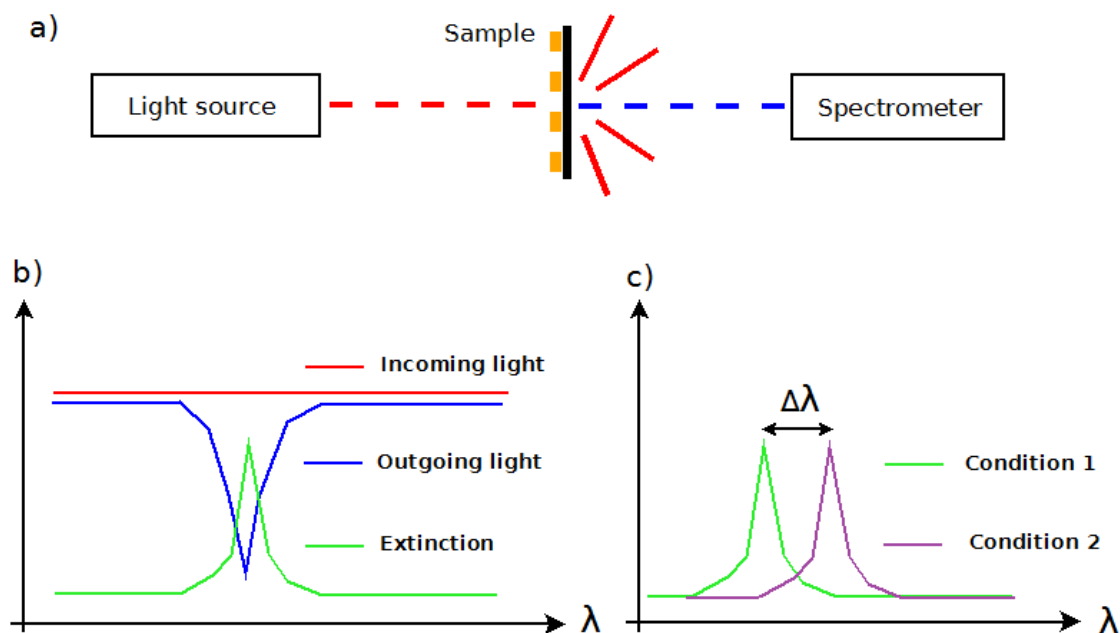
Figure 2.4: Basic setup and principle of LSPR sensing. a) Light is sent through a sample with metal nanoparticles, scattering or absorbing light close to the LSPR peak. **b)** The spectrum of the outgoing light is compared with an "undisturbed" reference signal (i.e. light passing through a blank sample) in order to find the resonance peak. **c)** Upon some physical/chemical changes the extinction peak shifts. The wavelength shift $\Delta\lambda$ may then be linked to some parameter (e.g. the hydrogen concentration). After calibration, $\Delta\lambda$ can thus be used to measure the aforementioned parameter.

for hydrogen sensors are vehicles as well as all facilities storing, producing or using hydrogen. However, a need for hydrogen sensors may also be found among other "new gas" applications (e.g. natural gas or methanol production) [4, 21].

Boon-Brett et al. performed a market survey, gathering specifications on commercially available sensors [22]. They also gathered the needs and requirements of automotive and stationary applications. Table 2.1 presents a summary of the requirements from car manufacturers. For stationary applications the requirements where obtained from the ISO/DIS 26142 specification, Boon-Brett summarised the requirements according to table 2.2.

Several types of hydrogen sensors have been commercialised. The most common type is electrochemical sensors, measuring the potential difference between an anode-cathode couple [22]. The anode reaction is the oxidation of hydrogen, thus relating the signal to the hydrogen concentration. Other common types are semiconductive (with a resistance

Table 2.1: Summary of requirements on hydrogen sensors as desired by automobile manufacturers. From survey presented in [22].

Parameter	Requirement
Measuring range	Up to $4\,\text{vol}\%$, Survivability to $100\,\%$
Detection limit	$< 0.1\,\text{vol}\%$
Response time $t_{90\%}$	$< 1\,\text{s}$
Recovery time $t_{10\%}$	$< 1\,\text{s}$
Ambient temperature	$[-40\,^{\circ}\text{C}, +85\,^{\circ}\text{C}]$
Ambient pressure	$[62,107]\text{kPa}$
Ambient humidity	$[0,95]\%$ relative humidity
Power consumption	$< 1\,\text{W}$
Life time	$6000\,\text{h}$
Accuracy	$\pm 5\,\%$

Table 2.2: Summary of requirements on hydrogen sensors for stationary systems according to ISO/DIS 26142 [22].

Parameter	Requirement
Measuring range	Up to $4\,\text{vol}\%$, Survivability to $100\,\%$
Detection limit	$< 100\,\text{ppm}$
Response time $t_{90\%}$	$< 30\,\text{s}$
Recovery time $t_{10\%}$	$< 60\,\text{s}$
Ambient temperature	$[-20\,^{\circ}\text{C}, +50\,^{\circ}\text{C}]$
Ambient pressure	$[80,110]\text{kPa}$
Ambient humidity	$[20,80]\%$ relative humidity
Accuracy	$\pm 25\,\%$ or $50\,\%$ depending on concentration

dependent on hydrogen concentration) and catalytic sensors. *COMB*, combined sensors, combine different technologies in order to broaden the operating range.

Concluding the survey, *Boon-Brett et al.* states a number of areas where improvement is needed. This includes higher operating temperature, lower operating pressure, lower response/recovery times and the possibility to operate at very high humidity and during condensation.

Fiber Optic Sensors

Most hydrogen sensors measure an electric signal, for example a voltage between two electrodes. This introduces electric wiring and the possibility of sparks in spaces where the risk of leakage and explosions are the actual reason for using the sensor. Using light, in optical fibres, as the signal would eliminate this risk. Optical fiber sensors usually include a thin film of palladium or another hydride-forming metal [23]. The optical properties, e.g. the reflectance, of palladium change upon hydrogen uptake. Light that has interacted with a thin film can thus be used as a sensor signal, measuring the change in intensity or spectrum with a device located elsewhere.

2.5 Palladium-Gold Alloy

Gold and palladium is a widely used alloy, mainly in jewellery [24]. Applications have also been found on the nanoscale, mainly due to improved catalytic effects compared to the pure metals. $AuPd_4$ alloy particles have been used for high selectivity of the H_2O_2 formation from H_2 and O_2 [25]. Substituting the core of Pd-particles with gold has proved favourable for catalysis of some reactions [26]. These improved catalytic properties are attributed to different electronic structures compared to the pure metals [26]. Such differences might also affect aspects of interest in this thesis, such as plasmonic and hydrogen uptake characteristics.

The combination of Au and Pd has proved to be well suited for optical hydrogen sensing. Examples of sensors implementing mixed PdAu are given in [21, 27] and a sensor implementing two separated layers of Pd and Au is presented in [28]. Most sensors using Pd and/or Au measure an intensity such as the reflectance of a thin film, as opposed to a spectrum or a wave-length as is typical for LSPR measurements. This introduces sensitivity to external intensity variations (e.g. a dust grain that blocks part of the light may affect the light intensity in the same way as a change in the hydrogen concentration).

2.5.1 Plasmonic Properties

Gold is one of the most commonly used metals for LSPR applications due to a sharp resonance frequency [29], seen as a narrow peak in the extinction spectrum. Palladium particles also exhibit LSPR, although with a much weaker and broader peak. Another difference is that, for particles with a diameter of $> 100\,\text{nm}$, the LSPR extinction is much more dominated by absorption in Pd, while absorption and scattering are of similar

magnitude in gold particles[29]. The high absorption cross section and wide peak are caused by a larger imaginary part of the complex dielectric function of Pd.

2.5.2 Characteristics of Hydrogen Uptake

Hydrogen uptake in both thin films and nanoparticles of palladium has been thoroughly investigated. Palladium is good at both catalysing the dissociation of H_2 [18, 30] and storing hydrogen [18]. Upon hydrogen uptake the plasmonic properties of Pd change, the LSPR frequency shifts linearly with the concentration of hydrogen inside the Palladium ($\Delta\lambda \propto C_H$) [18] and thus becomes an indicator of the external hydrogen pressure. However, when measuring the hydrogen concentration inside the palladium over a charge-discharge cycle, a hysteresis appears (see figure 2.5). The pressure plateau is located on different pressures, introducing ambiguity in the measurement.
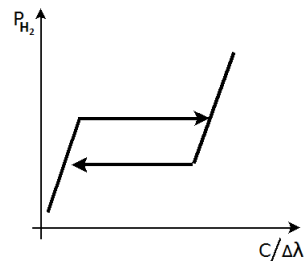
Figure 2.5: The LSPR wavelength shift $\Delta\lambda$ is proportional to the concentration C of hydrogen inside palladium and can thus be used as a signal for sensing hydrogen. However, a hysteresis between charge and discharge introduces ambiguity in the measurement of the external hydrogen pressure P.

Gold does not absorb hydrogen. However, a PdAu alloy may have many benefits when it comes to sensing. Measurements on thin films have shown that the hysteresis in the charge/discharge cycle gradually disappears when increasing the gold content [21]. This comes at the cost of a lower signal-to-noise ratio.

2.5.3 Fabrication, Structure and Alloying

As several thin-film PdAu sensors have been investigated, several methods of fabricating PdAu alloys on the nanoscale have been presented. This includes deposition through simultaneous sputtering [21], alternating evaporation [27] (layers of 1.6nm Pd and 0.6nm Au) and alloy target sputtering [31]. None of these techniques are available to this project, the ambition is to find a fabrication technique that only requires deposition of one pure layer of each metal. Annealing might be the solution for this. Annealing has proved to have a considerable impact on the hydrogen uptake characteristics of PdAu particles. In [31], a 20 nm thick film of $Pd_{0.6}Au_{0.4}$ was annealed at different temperatures, yielding up to $6\times$ enhancement in the optical signal (reflectance) used for hydrogen sensing. However, this does not guarantee the possibility of migration and mixing of two thick layers of metal.

Ferrando et al. [26] presented and reviewed several studies of PdAu nanoparticle synthesis, mainly through chemical fabrication methods. They state that "segregation properties of Pd-Au nanoparticles seem to be far from simple.". The majority of the studies found an $Au_{core}Pd_{shell}$-structure favourable, although a Molecular Dynamics simulation of PdAu freezing found $Pd_{core}Au_{shell}$ to be the most stable. One group reported $Au_{core}Pd_{shell}$ particles being stable up to at least $500\,^{\circ}C$ while other report homogeneous mixing at $300\,^{\circ}C$. The presence of oxygen seems to have a major influence on the structure as oxygen binds to surface Pd at above $300\,^{\circ}C$, forming PdO. Heating of bulk PdAu alloys in O_2 has been proved to lead to surface enrichment of Pd (or rather PdO).

3

Method

3.1 Fabrication

3.1.1 Hole-Mask Colloidal Lithography

In order to study plasmons and other behaviour in metal nanoparticles, disk-shaped particles are often used. For this purpose a special fabrication method has been developed, called hole-mask colloidal lithography [32]. Self-organising charged colloidal particles are used to transfer a pattern of sparse disks onto a substrate. The process is illustrated in figure 3.1

The substrate of choice (typically Borosilicate glass or silicon) is initially cleaned using three solvents (isopropanol, aceton and methanol) in an ultrasonic cleaner. A layer of the polymer PMMA is added to the surface by spin-coating and heating. The PMMA is exposed to an oxygen plasma for a short time in order to make the surface more hydrophilic. The surface is made positively charged by adding a layer of the poly-electrolyte PDDA. A solution containing negatively charged, spherical colloidal particles is then added. Due to the charge, the spheres organise in a sparse pattern. The size and pattern of these particles will determine the size and pattern of the metal disks.

A 20 nm layer of gold is deposited by e-beam evaporation. The colloidal particles are then removed by tape-stripping, leaving circular holes in the gold. The sample is placed in an oxygen plasma, etching the PMMA that is not covered by gold, thus creating (approximately) cylindrical holes with size and location according to the colloidal particles used.

The next step differs somewhat depending on the particle composition. Through the mask, whatever metal that is desired can be deposited. After deposition, the gold mask is lifted off by desolving the PMMA in acetone, leaving only disk-shaped particles on the substrate.
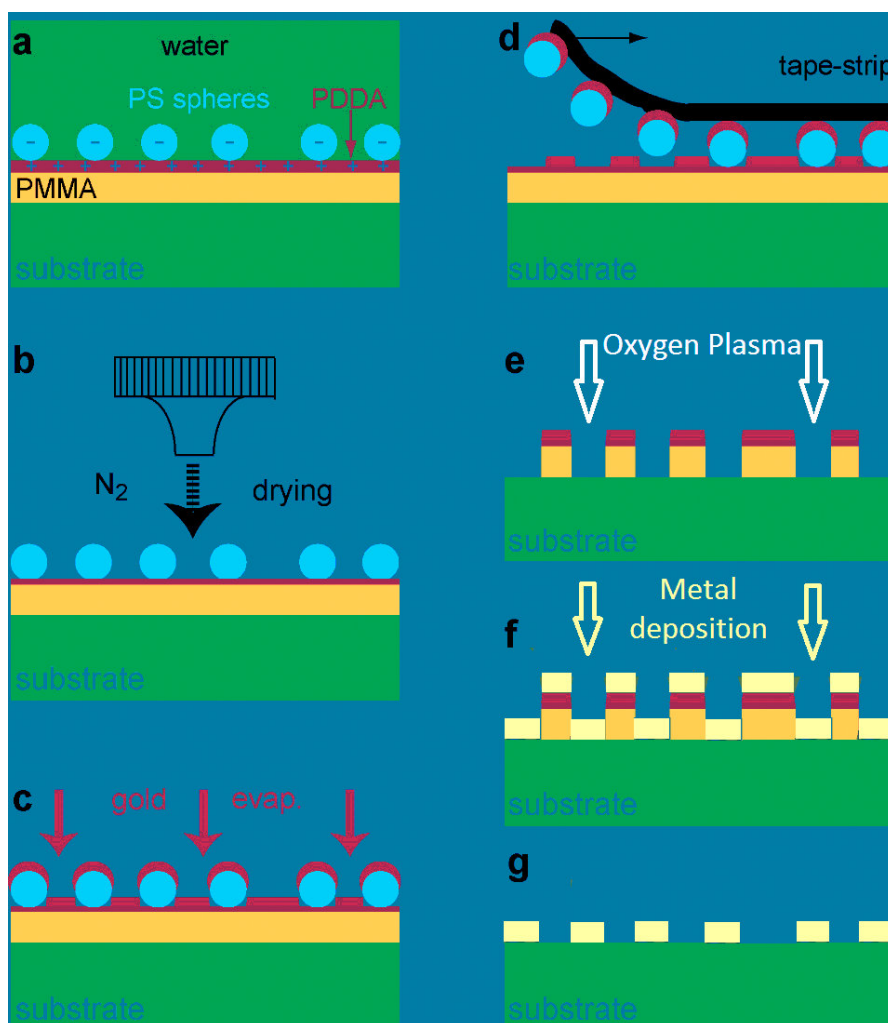
Figure 3.1: The main steps of Hole-Mask Colloidal Lithography. **a)**
Charged colloidal particles are added to a surface covered in PDDA and PMMA. The
particles stick to the PDDA thanks to the electrostatic attraction and organise in a
sparse pattern due to the repulsion between particles. **c)** Gold is deposited on top of
the particles and the substrate. **d)** The particles are removed by tape stripping leaving
a gold mask. **e)** An oxygen plasma is used to etch holes into the PMMA according to
the mask. **f)** Metal is deposited through the mask. **g)** The mask is lifted off using
acetone, leaving disk-shaped particles.
Figure modified from *Christoph Langhammer*.

3.1.2   Palladium-Gold Fabrication

The fabrication of the Pd-Au alloy nanoparticles consists of two steps:

1. Deposition through the mask explained in 3.1.1 with a layer of Au and a layer of

Pd. After the lift-off we thus have heterogeneous disks.

2. Annealing (heating) the disks in order to promote mixing/alloying of the metals.

The deposition through the mask is done using the E-beam evaporator *Lesker PVD 225*. In vacuum ($P < 5 \cdot 10^{-7}$ Torr), a beam of electrons is directed towards a target of Pd or Au. The target is heated up and starts to evaporate, coating all exposed surfaces in metal. A QCM (Quartz crystal microbalance) is used in order to record the thickness of the deposited layer and to control the deposition rate. The substrate (in our case the gold mask) is initially covered by a shutter that opens when the deposition rate is $\approx 1 \text{Å}/s$. The shutter is closed when the specified thickness has been reached. It takes a certain time for the shutter to open/close, introducing an uncertainty in the deposited thickness. This is estimated to $\pm 2 \text{Å}$, corresponding to a range of $17.1 \, \text{at}\% < [\text{Au}] < 18.6 \, \text{at}\%$ when evaporating Au and Pd with specified thickness $5 \, \text{nm}$ and $20 \, \text{nm}$.

As the metal is deposited through the mask onto the substrate, the atoms also bind to the gold. This decreases the diameter of the gold mask at about the same rate as the height increases, leading

3.2 Plasmonic Measurements

In the last chapter we discussed the principle behind plasmonic sensing. In this project, three different setups were used where the extinction spectrum could be analysed under different circumstances.

As explained in section 2.3, the plasmonic nanoparticles create an extinction spectrum with a peak at a certain wavelength. In order to analyse the change of the spectrum a set of signals has been used. A function is first fitted to the spectrum, either a polynomial(in the case of the *X1 reactor*) or a Lorentzian on the form obtained from (2.3) and (2.4). Three signals are then obtained from the fit, illustrated in figure 3.2. The peak position signal is trivial, the wavelength/position of the highest point of the fitted spectra. This project often used an alternative signal, the *centroid*. It can be described as the "centre of mass" of the spectrum (see [33]or [34] for a more detailed description) and the usage of it usually results in less noise. The centroid wavelength will be close to the peak position but with a slight offset as the shape of the spectrum peak is somewhat asymmetric.

When the peak lies close to the edge of the analysis range, the centroid might be impossible to calculate or noisy. In such cases the extinction at the peak (denoted as *ext@peak*) has been used to monitor the process. It is simply the highest extinction found in the spectrum.

3.2.1 X1 Reactor - Annealing and Hydrogen Gas Mixtures

The X1 reactor was used for most of the measurements presented in this thesis. Its ability to accurately control the gas content and temperature made it suitable for both annealing and measuring of isotherms.
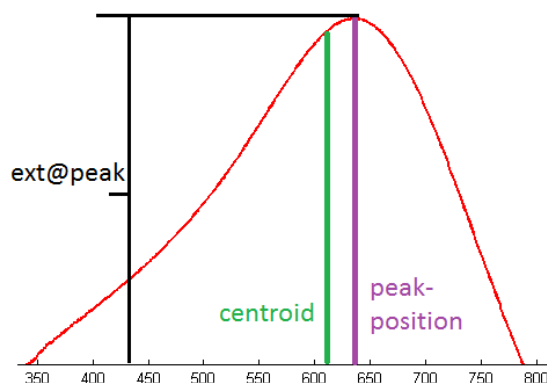
Figure 3.2: Illustration of he signals that have been used in order to monitor the changes in the LSPR extinction spectra. A Lorenzian or polynomial is first fitted to the curve. Then the position of the peak, the extinction at this position and the centroid ("centre of mass") are obtained. Note that the centroid is somewhat shifted relative to the peak due to the "heavier" left side of the spectrum.

The *Insplorion X1 reactor* (see figure 3.3) consists of a quartz tube (containing $\approx 200\,\text{mL}$ gas) with access ports for incoming white light and outgoing light for analysis of the extinction of the sample. The incoming light originates from a halogen lamp and the outgoing light is sent to a spectrophotometer, both controlled by a computer. In the middle of the quartz tube two samples can be mounted for individual LSPR sensing.

In one end the tube is connected to an exhaust pipe of atmospheric pressure, in the other it is connected to programmable gas valves. These valves are supplied with pressurised gases that are released at a rate controlled by the computer. Two valves were used, one for argon and one for a mixture of hydrogen gas and argon ($4\%\text{H}_2$). Only argon is used during annealing. During all measurements using hydrogen, a constant flow of $150\,\text{mL/min}$ is maintained while varying the content of the two gases between $0\%\text{H}_2$ and $4\%\text{H}_2$. As the flow is $150\,\text{mL/min}$ and the volume $\approx 200\,\text{mL}$, the time it takes to exchange the gas of the chamber is of the order of 1 minute.

The quartz tube is surrounded by a heating coil and covered with insulation. Thermocouples are used for monitoring the temperature of the gas and of both samples. The temperature of the gas is controlled from the computer with a fairly fast heating rate but a slower cooling. A typical heating curve for an annealing sequence can be seen in figure 3.4. When annealing, the setpoint for the temperature is set at the annealing temperature. A timer starts when the temperature of the gas has reached the setpoint, this timer is referred to as the annealing time. When the timer runs out, the sample is left to cool in a $300\,\text{mL/min}$ Ar flow. Note that the sample stays at a fairly high temperature during a longer time than the specified annealing time (typically $\approx 1\,\text{h}$ before reaching $T < 50\,^\circ\text{C}$).

The LSPR measurement is performed using the software *Insplorer 1.1*. First, a reference sample (clean Borofloat glass) is placed in each sample holder and the spectrum is recorded. The extinction of the particles can then be obtained by replacing the reference
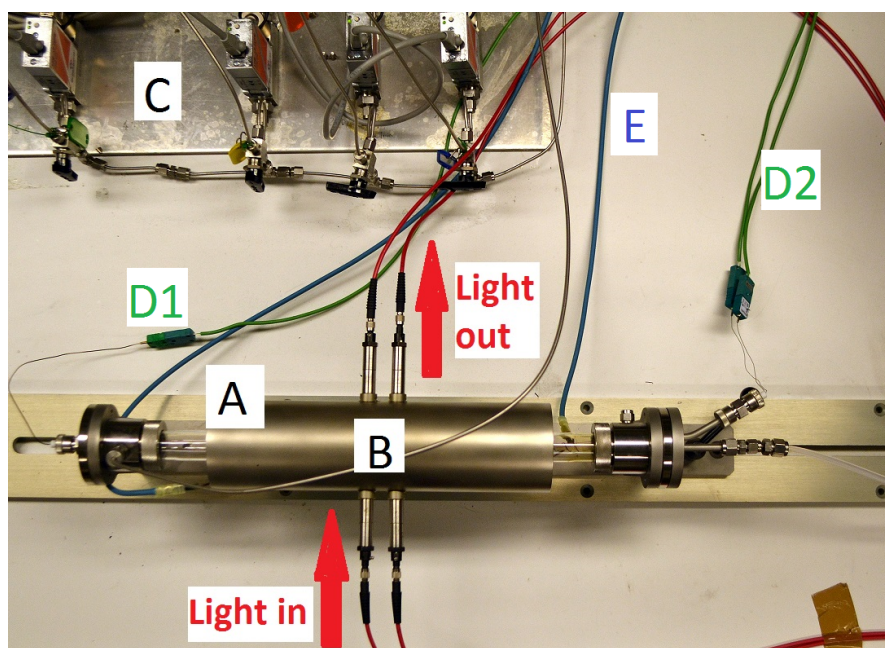
Figure 3.3: Insplorion X1 reactor, the setup used for annealing and hydrogen isotherm measurements. **A)** Quartz tube containing the samples and the gas mixtures. Under the metal cover the tube is surrounded by a heating coil **(E)** and covered by insulation. **B)** Two samples are located in the middle of the tube, each aligned with one optic fiber for incoming light and one fiber for outgoing light. **C)** Valves for control of the gas flow, one is used for Ar and one for H_2. **D)** Thermocouples are monitoring the temperature of the gas (1) and the samples (2).

sample and dividing the spectra. The software controls the gas flow and temperature according to a program, simultaneously recording the extinction spectra. The software analyses the spectra by fitting a polynomial to the points and calculating the position of the peak, the centroid and the *ext@Peak* signals.

The reactor was very useful for annealing and for measuring isotherms as it is easy to accurately vary the temperature and the H_2 concentration. The main downside is the inherently slow response time (estimated to $\approx 30\,\text{s}$) due to the time it takes to completely replace the gas of the reactor.

Isotherms

In the context of metal hydrides, *isotherm* refers to the relation between the external hydrogen pressure P_{H_2} and the hydrogen content in the metal C_{H_2} at constant T. In our case, isotherms have been measured with an LSPR signal instead of the hydrogen content on the x-axis. This signal is expected to be proportional to C_{H_2} and should thus show the main features of the P_{H_2}-C_{H_2} curve, such as the pressure plateau and hysteresis.
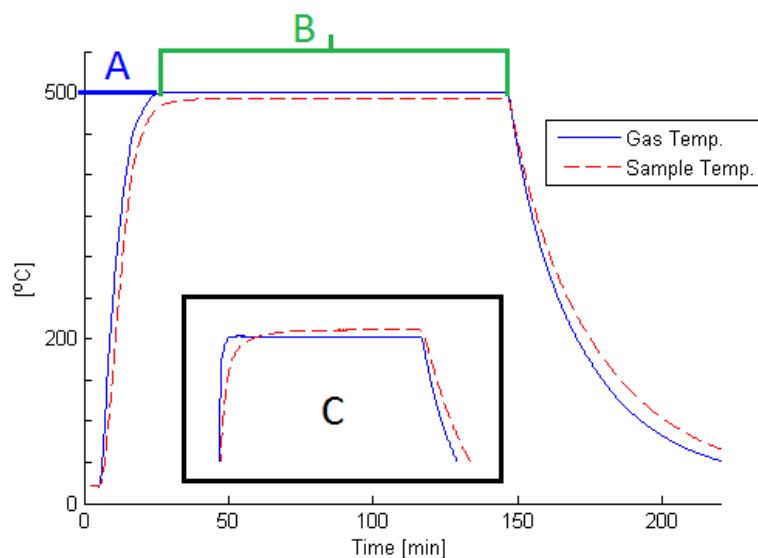
Figure 3.4: Typical heating curve in the X1 reactor and definitions for annealing. **A)** The annealing temperature is defined as the setpoint of the gas temperature, 500 °C in this case. Note that the actual sample temperature deviates from this value. **B)** The annealing time is defined from the point where the setpoint is reached until the heating is cancelled, 2 hours in this case. Note how the sample stays at a fairly high temperature for some time after the two hours. **C)** Note how in the case of 200 °C, the sample temperature is higher rather than lower compared to the gas temperature.

The gas flow curves during the isotherm measurement can be seen in figure 3.5. While maintaining a constant flow of 150 mL/min, P_{H_2} is increased in steps by varying the ratio of the flow from the valves containing pure Ar and 4%H$_2$. Every step lasts five minutes. The gas flow ratios and the signal of choice (*ext@peak* or *centroid*) are recorded. The hydrogen concentration is plotted in *Matlab* and a point at the end of each 5 minute step is chosen as a data point in the isotherm.

The isotherm measurements are always preceded by at least 5 fast hydrogenation cycles in order to stabilize and relax the particles. These cycles consist of 5 minutes with a flow of 4% H$_2$ and 5 minutes of pure Ar flow.

3.2.2 Vacuum Cell

In order to measure the response time of the sensor, a fast enough response time for the hydrogen pressure is needed. As this could not be provided by the X1 reactor (see last section), a vacuum cell (see figure 3.6) was used for this purpose. This vacuum cell consists of a stainless steel chamber with a small volume. Two manual valves connect the chamber to either a turbopump or a pipe containing pure H$_2$ gas. Light is sent through the sample to a spectrometer and analysed using a *Matlab* program. The temperature of the sample is monitored by a thermo couple.

The pipe connected to the chamber is first filled with hydrogen manually from a pres-
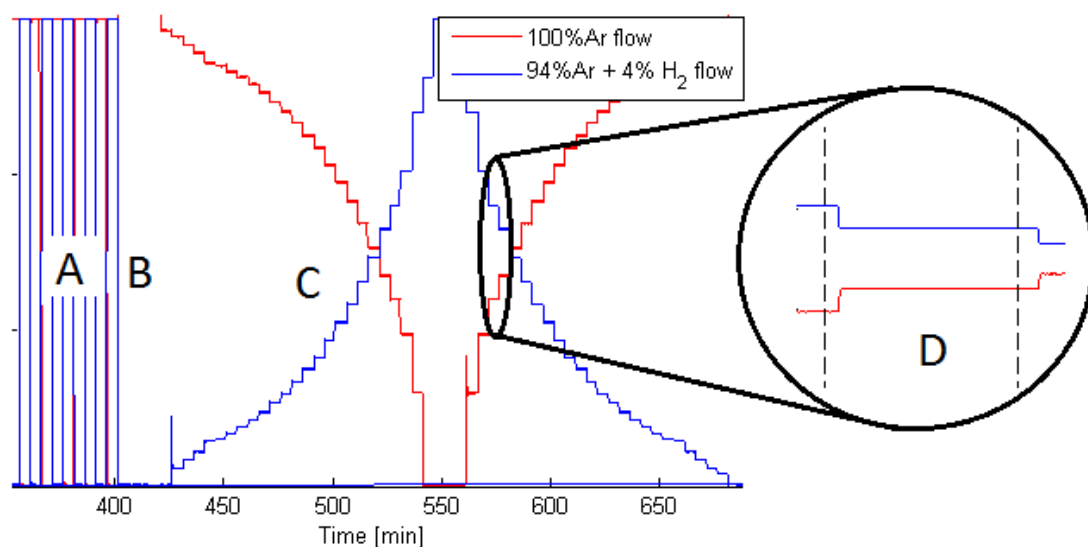
Figure 3.5: Gathering data for a hydrogenation isotherm. **A)** Initially 5 fast steps of 4% hydrogen are run in order to stabilise the particles. **B)** argon is flushed at a high rate in order to clear out all hydrogen. **C)** The hydrogen concentration is increased/decreased in steps of 5 minutes. **D)** At the end of each step a data point is chosen manually, the corresponding LSPR signal value is also noted.
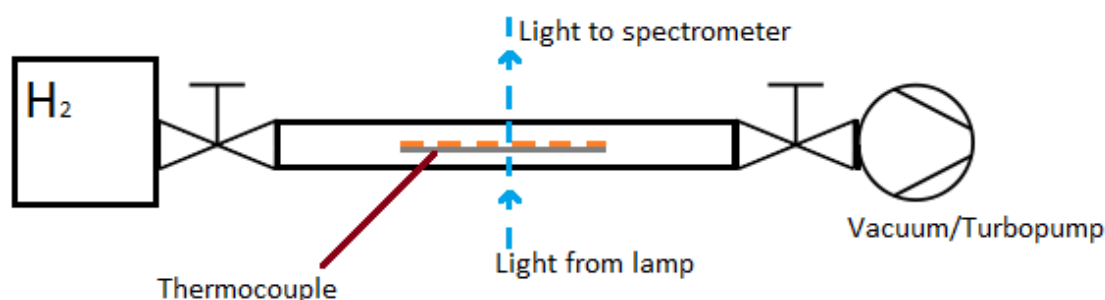
Figure 3.6: A sketch of the vacuum cell setup used for measurements with a high temporal resolution. The sample is placed inside a small steel tube. Via manual valves, the tube is connected to a turbo pump in one end and to H_2 gas ($P \approx 0.1 - 1$atm) in the other. A thermocouple is in contact with the sample and the optical analysis is performed using light sent via optical fibres connected to the steel tube.

surised bottle. The pressure can be monitored up to ≈ 1 bar. An absorption/desorption cycle is performed by first opening the valve and letting gas from the pipe flow into the sample chamber. The absorption is assumed to be completed when the optical signal has stabilised. The valve to the turbopump is then opened, creating vacuum ($< 10^{-4}$ bar) within 5 seconds. A small leak is believed to exist as a small change in optical signals, corresponding to increased pressure, has been observed after closing the valve to the

turbopump. This rise is regarded as negligible.

3.2.3 Cary

For a few measurements the spectrophotometer *Cary 5000* from Agilent Technologies was used. It has high resolution, high precision and can produce accurate extinction spectra in a broader wavelength range than the spectrometer used together with the X1 reactor. However, no heating or H_2 exposure was possible and the system was thus only used to produce spectra under static conditions in air.

3.3 SEM Analysis

An SEM was used throughout the course of the project for qualitative analysis of the particle shape, verification of the fabrication as well as quantitative analysis of the particle size.

Scanning Electron Microscopy is an imaging technique utilizing the short wavelength of electrons to obtain resolutions down to the order of 1 nm [35]. The microscope sweeps an electron-beam in a pattern over the surface, simultaneously measuring some signal for every "pixel" and thus forming the image. The most common signal is *SE* (secondary electrons), electrons emitted by excited atoms at the surface. The signal is very surface sensitive, originating from atoms within a few nanometers of the surface.

For the work of this thesis a *Carl Zeiss AG - SUPRA 60VP* microscope was used. Most images were obtained from *SE* using the *In-lens* detector of the microscope. At optimal working distance the resolution is 1.6 nm at an acceleration voltage of 1 kV and 0.8 nm at 15 kV [36]. The voltage used for most images in this thesis was 8 kV.

The sample could be placed in different types of holders depending on the purpose of the imaging. For size determination a flat sample holder was used. In order to see the shape of the particles, a tilted image could be obtained by mounting the sample in a holder with grooves tilted 70°.

3.3.1 Image Analysis for Size Distribution

An important role of the SEM was to analyse the size distributions of the particles. This provided a way of comparing the quality of fabrication batches and to estimate the effect of the annealing on the shape of the particles.

In order to determine the size distribution of a sample, images were taken at $10^5 \times$ magnification with a working distance of 5 mm. The software *ImageJ* [37] was then used in order to analyse these images.

The analysis of the size distribution was performed by finding all pixels of an image with a brightness over a certain threshold (see the red areas of figure 3.7). This threshold brightness was chosen manually, trying to cover the particles but nothing more, thus introducing a possible error or bias due to the "human factor". Still in *ImageJ*, these areas could then be interpreted as particles, all areas with circularity and size over certain values were regarded as particles.
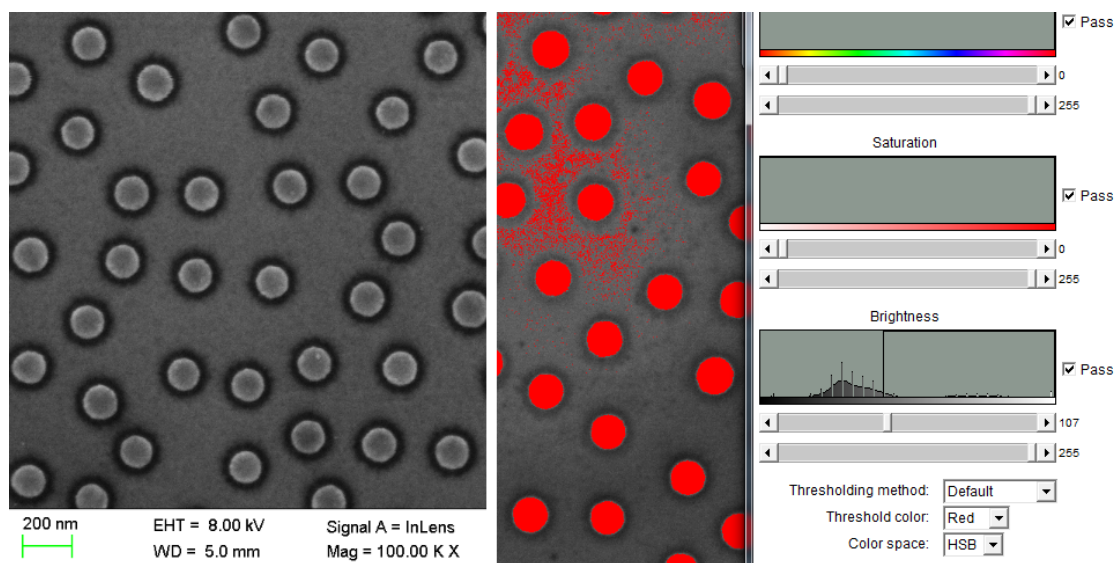
Figure 3.7: Determining the size of particles in an SEM image. **Left:** An image obtained from the SEM, with the scale in the down-left indicating the number of pixels per length. **Right:** Marking the particles by tuning a threshold brightness. Red areas of certain size and circularity are considered particles and will be measured.

ImageJ produced data in the form of area (in units of pixels) of the particles. Assuming perfectly circular particles the area could be transformed to a diameter. The pixel units were translated to nm using the scale in the lower left part of figure 3.7.

3.4 XPS Analysis

X-ray photoelectron spectroscopy [38, 39] provided a way of analysing the chemical composition at the surface of the samples. The technique is based on the photoelectric effect. In ultra high vacuum, the sample is exposed to x-rays of a known energy, the excited atoms emit electrons that are collected in an electron lens for analysis. By counting the number of electrons per energy interval a spectrum is obtained, showing peaks at the electron binding energies of the present elements.

Due to the short mean free path of electrons inside a solid the method is very surface sensitive, the peaks of the spectra represent electrons from within tens of angstrom below the surface [39]. As the palladium layer of the particles is much thicker ($\approx 180\text{Å}$) this thus becomes an indicator of whether the metals have been mixed and the gold has migrated to the top. The surface sensitivity can be increased further by tilting the sample relative to the electron collector. If the electrons need to leave the sample at a high angle they will pass through more material, making collision more probable and the effective analysis depth shorter.

The system used was equipped with an Al Kα x-ray source. It also provides an electron beam source. This is needed as the sample otherwise gets charged when emitting
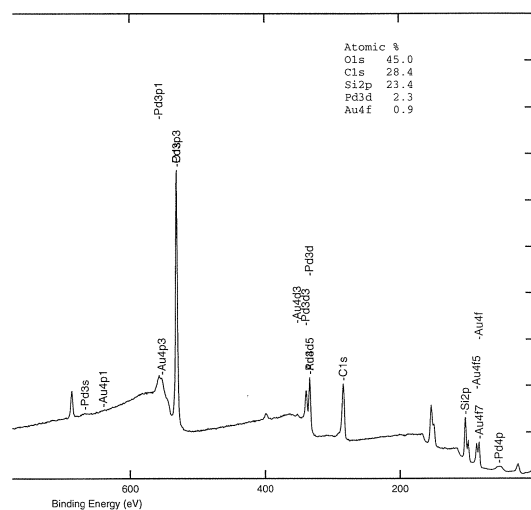
Figure 3.8: A typical XPS spectrum of PdAu nanodisks. Show the main peaks of C (≈ 290 eV),O (≈ 530 eV), Si (≈ 100 eV), Au(≈ 85 eV) and Pd (≈ 340 eV). The list of content of each element was obtained using *Multipak*.

electrons. After mounting the sample, the first step is to tune the current from this electron beam in order to match the rate at which electrons are emitted from the sample. This is done by observing the primary peak of carbon and adjusting the current until the peak is located between 285 eV and 288 eV, typical binding energies of the 1s electron in the most common carbon-containing compounds.

The measurement is then performed by counting electrons for each part of the spectrum. The analysis is carried out using the software *Multipak*. Taking into account the particles, the substrate and contamination, each sample was assumed to contain the elements C (main peak at ≈ 290 eV),O (≈ 530 eV), Si (≈ 100 eV), Au(≈ 85 eV) and Pd (≈ 340 eV). Multipak indicated the primary peaks of these elements and a baseline was then chosen manually, separating the peak from the background. Based on the area of each peak, Multipak calculated the content of each element. A typical result can be seen in figure 3.8.

4

Results

The results are presented in an order that answers the research questions in a natural way. First, some aspects of the annealing will be presented. Then the effects of the annealing will be analysed by XPS and SEM results. Last, the hydrogen uptake measurements will be presented.

4.1 Annealing

The particles are annealed in order to promote mixing and alloying between Au and Pd. This has a central role in the project as one of the main questions is whether alloying is possible with the equipment and methods at hand. The samples were annealed using the X1 reactor as explained in section 3.2.1. The annealing was monitored by recording changes of the LSPR peak position. Many factors may influence this signal other than alloying, such as particle geometry change and the temperature itself. Alloying can thus not be verified only by this measurement but it can give a hint about at what temperature atoms become mobile.

In figure 4.1 annealing curves for two different temperatures are presented. Note how the plasmon peaks have changed irreversibly for both temperatures, indicating a structural/geometrical change. Note also that the magnitude differs between the two temperatures and how the peak seems to drop additionally just before the temperature reaches $500\,^\circ$C.

In order to verify whether the change of the plasmonic peak can be attributed primarily to alloying, pure Pd particles were analysed. In figure 4.2 annealing curves for PdAu particles are compared with pure Pd particles. Note that the peak shift is even larger for the pure Pd particles, for which alloying can be excluded as a factor.
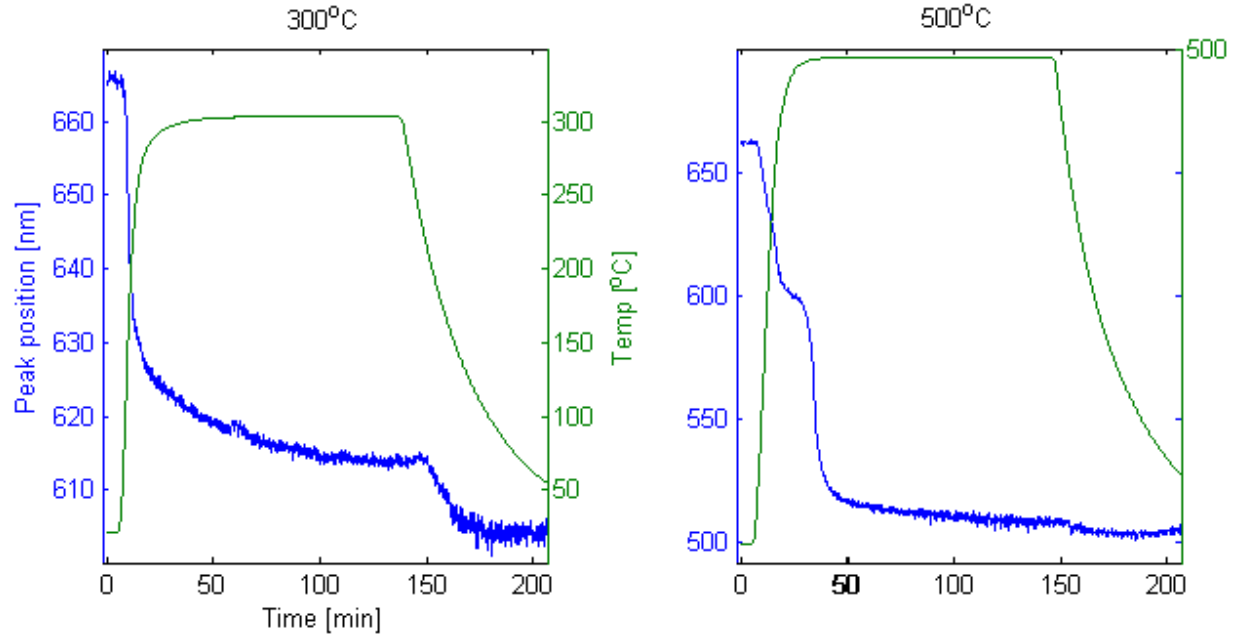
Figure 4.1: Annealing curves for $Pd_{81}Au_{19}$ particles at different temperatures. The blue signal is the peak position of the LSPR spectrum. Particle dimensions are $D \approx 100\,\mathrm{nm}, h \approx 20\,\mathrm{nm}$.
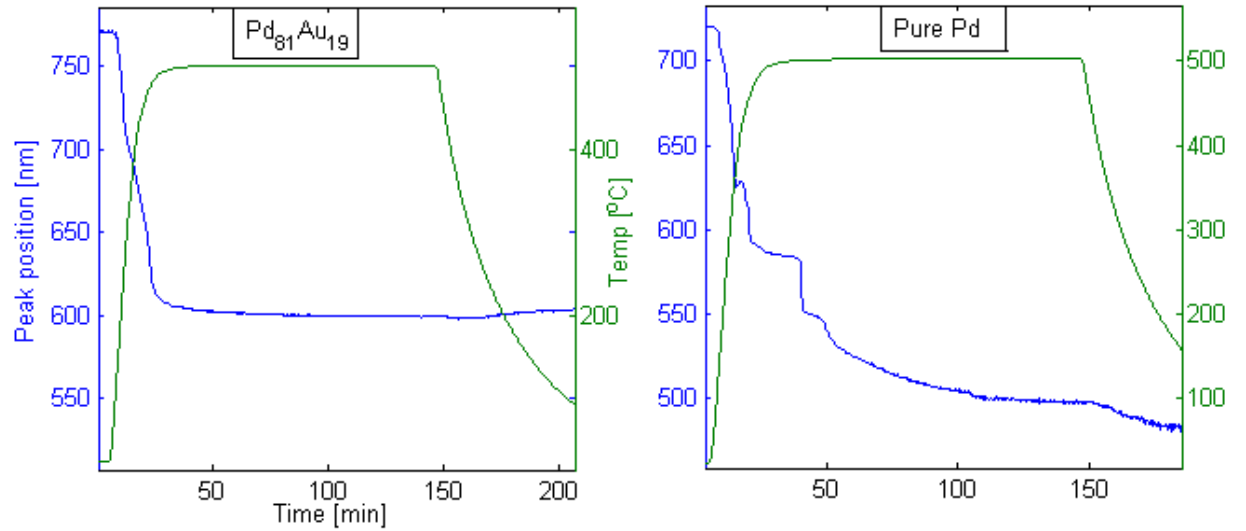
Figure 4.2: Annealing curves for $Pd_{81}Au_{19}$ and pure Pd particles. Both samples were annealed in $500\,^{\circ}\mathrm{C}$ for $2\,\mathrm{h}$ at the same position in the reactor. The blue signal is the peak position of the LSPR spectrum. The total peak shifts are $\Delta\lambda_{\mathrm{PdAu}} \approx 170\,\mathrm{nm}$ and $\Delta\lambda_{\mathrm{Pd}} \approx 240\,\mathrm{nm}$. Particle dimensions are $D \approx 190\,\mathrm{nm}, h \approx 25\,\mathrm{nm}$.

25

4.2 SEM

The size of the nanodisks is determined using Scanning Electron Microscopy(SEM). This provided a way to both verify the result of the fabrication and investigate the effect of annealing.

The first particle size to be used was 100 nm. Particles of this size proved to have a very low peak wavelength, making analysis difficult as the peak was located below the measurement range of the instruments. An SEM image can be seen in figure 4.3. Several such images were analysed using *ImageJ* as explained in section 3.3.1, resulting in a size distribution showed in figure 4.4(a). This can be compared to the second batch, fabricated using polystyrene spheres of size $D \approx 140$ nm instead. As seen in figure 4.4(b) the distribution is considerably more narrow with a standard deviation of $\sigma = 7.3$ nm compared to the 100 nm particles for which $\sigma = 17$ nm. Together with the a wavelength better matching the measurement range of the detector, this might improve the quality of the LSPR measurements as a narrow size distribution is expected to result in a more narrow extinction peak.

As was mentioned in section 4.1 the blue-shift of the peak upon annealing might be (entirely or partially) due to a change in particle geometry. To investigate this geometry change, the 140 nm sample was studied in the SEM before and after annealing at 400 °C. The images were once again analysed in *ImageJ* and the result can be seen in 4.4. The same was done for particles of $D \approx 190$ nm annealed at 500 °C, as can be seen in figure 4.5. For both samples, the particle diameter seems to have decreased upon annealing.
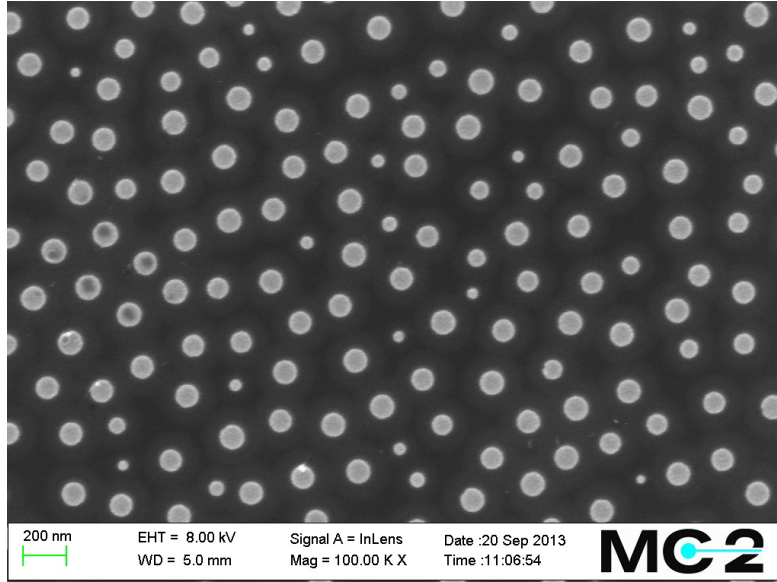
Figure 4.3: SEM image of PdAu nanodisks fabricated using polystyrene spheres with $D \approx 100$ nm. Note the size dispersion of these particles.

(a) 100nm.

(b) 140nm, Unannealed.

(c) 140nm, Annealed.
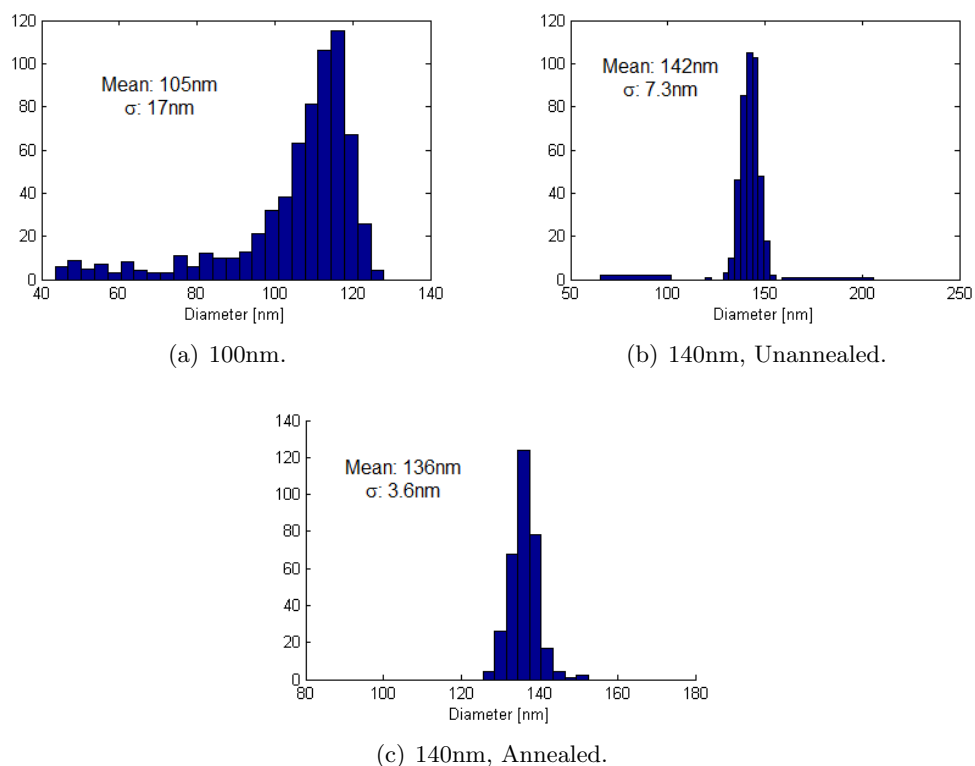
Figure 4.4: Size distribution of PdAu nanodisks fabricated using polystyrene spheres with $D \approx 100\,\text{nm}$ and $140\,\text{nm}$. The size distribution was obtained from SEM images (such as figure 4.3) using *ImageJ*. Note the larger dispersion of the smaller particles.

(a) 190nm, Unannealed
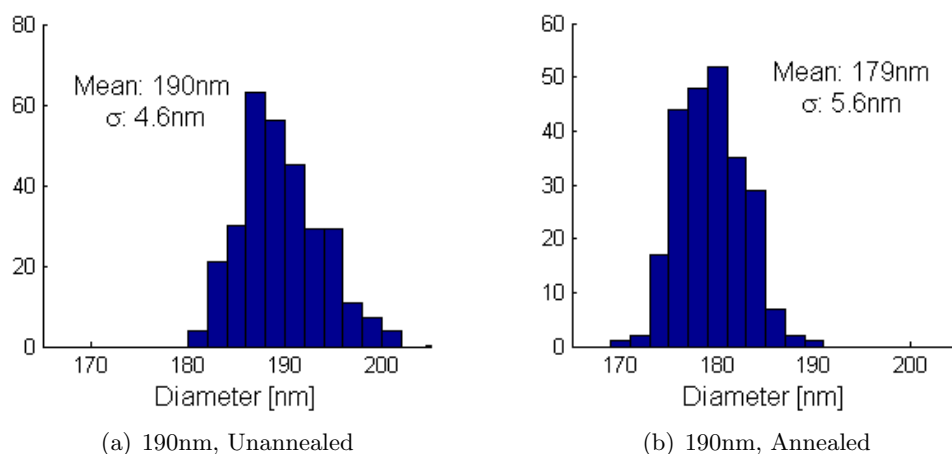
(b) 190nm, Annealed

Figure 4.5: Size distribution of PdAu nanodisks fabricated using polystyrene spheres with $D \approx 190\,\text{nm}$. The sample was annealed at $500\,^{\circ}\text{C}$, $2\,\text{h}$. Note how the mean diameter has decreased during annealing.

4.3 XPS Analysis

A typical result of an XPS measurement can be seen in figure 3.8. In this section I will not present the detailed individual XPS-spectra but will focus on the concentrations of gold and palladium within the particles. These concentrations are calculated according to

$$[Au]_{XPS} = \frac{[Au]'}{[Au]' + [Pd]'} \tag{4.1}$$

where $[Au]'$ is the concentration of Au according to the raw data (including substrate, particles and contamination) and $[Au]_{XPS}$ is the concentration within the particle surface.

The first measurement was performed on a thin film. This was done in order to increase the proportion of the signal from gold and palladium compared to the substrate, since for particle samples the surface coverage is only around 10%. However, the thin film proved unsuitable for analysis of the effect of annealing, the main reason for using the XPS system. Upon annealing, the film was deformed as the atoms clumped up in small particles, unrepresentative for the particle shape of interest.

Two particle samples were also tested, one for which gold was deposited on top of the Pd and one for which it was deposited at the bottom of the particle. Annealing seems to have had a significant effect on both. The sample with gold deposited at the bottom showed a low gold content at the surface before annealing (some gold should be visible from the side of the disk-shaped particles). After annealing, the gold content had changed significantly, with a Pd-Au ratio very close to what was deposited. The results from these measurements are summarized and presented in table 4.1.

In order to further verify the homogeneity, measurements were carried out for different angles between the sample and the electron collection lens. This alters the surface

Table 4.1: Summary of results from XPS measurements. $[Au]_{deposited}$ corresponds to the values that were specified to the evaporator as the disks/films were deposited. Top/bottom indicates whether the Au layer was deposited on top of or before the Pd. The gold content from the XPS results was calculated by the software *Multipak*.

Sample	$[Au]_{deposited}$	$[Au]_{XPS}$
21.6nm Film. Unannealed.	15 at% bottom	2.2 at%
21.6nm Film. Annealed 400 °C, 2h.	15 at% bottom	42 at%
Disks ($D = 140$ nm, $h = 20.4$ nm). Unannealed.	16 at% top	60 at%
Disks ($D = 140$ nm, $h = 20.4$ nm). Annealed 400 °C, 2h.	16 at% top	29 at%
Disks ($D = 190$ nm, $h = 20$ nm). Unannealed.	19 at% bottom	4.8 at%
Disks ($D = 190$ nm, $h = 20$ nm). Annealed 500 °C, 2h.	19 at% bottom	24 at%

sensitivity, as explained in 3.4, and should thus alter the influence of a deviating surface composition. The result of such a measurement can be seen in figure 4.6. Note that the detected gold concentration varies much less for the annealed sample.

Finally, one might notice that the gold concentration detected by the XPS for all annealed samples (both in figure 4.6 and table 4.1) is somewhat higher than the "deposited" gold concentration. This could point either to surface enrichment of gold or simply to the fact that the deposition leaves a higher gold concentration than what is specified.
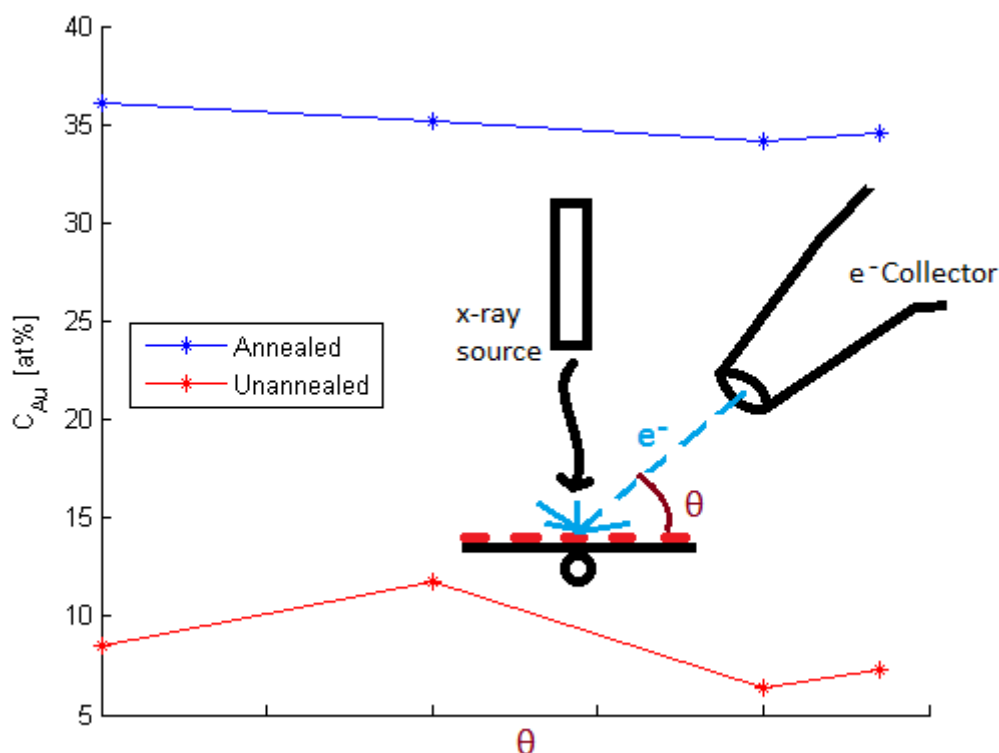
Figure 4.6: The gold concentration of the particles, as detected by the XPS system at different angles. The measurement was performed on $Pd_{73}Au_{27}$ particles (gold deposited on the bottom) of dimensions $D \approx 190\,nm, h \approx 25.7\,nm$. The annealing was done in $500\,^{\circ}C, 2\,h$. The surface sensitivity varies with the tilt and different results should thus be seen if the sample is inhomogeneous around the surface. When measuring on disk-shaped particles the influence from the sides of the disks also varies with the tilt. Note the lack of numbers on the θ-axis. No specifications for the exact angles of the instrument could be found.

4.4 Hydrogen Uptake

4.4.1 Isotherms for Varying Annealing Temperatures

In order to verify the mixing and alloy formation as well as the assumed consequences (smaller hysteresis), isotherms were measured for samples annealed at different temperatures. Isotherms show the relation between the hydrogen pressure and some LSPR signal during hydrogen uptake and release. The isotherms were plotted using data points from curves of the same type as figure 3.5. For some measurements the *ext@peak* showed lower signal-to-noise ratio than the centroid. This was thus used to plot the isotherms of these samples. However, for later samples the conditions were optimised in order to yield a clear centroid signal.

In figure 4.7 isotherms are plotted for samples annealed at three different temperatures, seemingly showing a decreased hysteresis for higher annealing temperatures. In order to slightly counter the blue-shift that occurs upon annealing, particles with the somewhat larger mean diameter 150 nm were used before measuring at higher temperatures. Figure 4.8 presents isotherms for samples annealed during 2 h at up to 500 °C as well as a comparison of the hysteresis. The figure also includes one sample that was annealed at 400 °C during 8 h. The hysteresis of this sample is clearly lower than of the sample annealed at 400 °C, 2 h but slightly higher than the one annealed at 500 °C, 2 h (0.16% vs 0.11%). The 600° sample seems to show a narrow hysteresis, note however that this measurement suffered from noise comparable to the hysteresis. Note that it was measured at a later occasion, perhaps under slightly different conditions (e.g. a different lamp, different setup for the optics et cetera.).
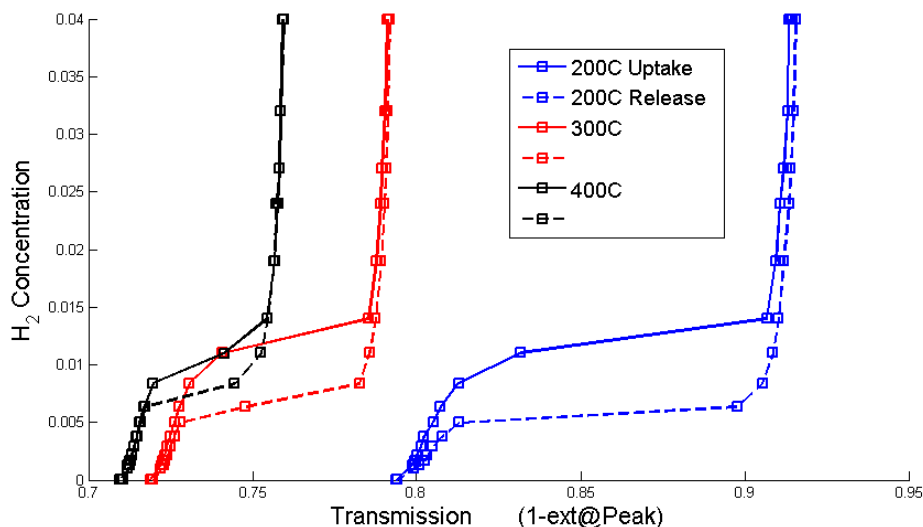
Figure 4.7: Isotherms for $Pd_{84}Au_{16}$ particles with $D \approx 140$ nm annealed during 2 hours at different temperatures. The signal used is the transmission at the peak wavelength, calculated as $(1 - ext@peak)$. Measured at 20 °C in a mixture of Ar and H_2.
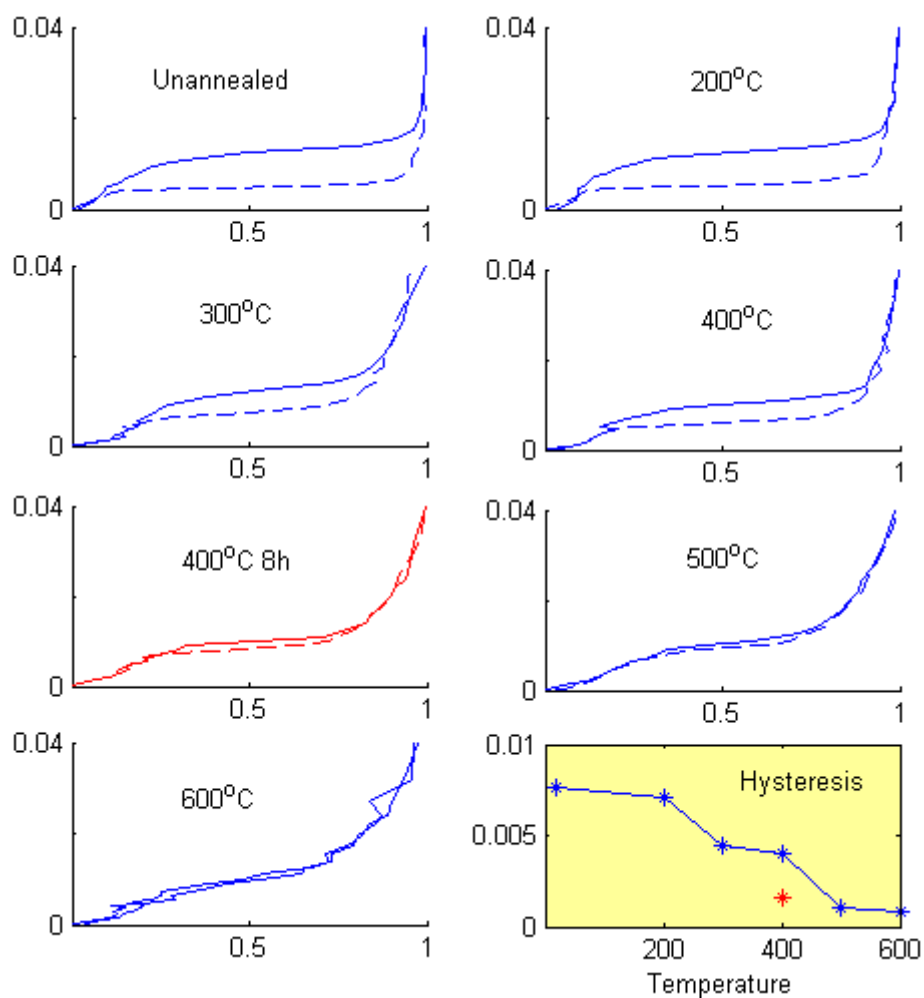
Figure 4.8: Figures 1-7: Hydrogen absorption/desorption isotherms for $Pd_{81}Au_{19}$ particles with $D \approx 150$ nm annealed during 2 hours (red curve 8 hours) at different temperatures. The y-axis shows the hydrogen content of the gas mixture (i.e. the hydrogen pressure in bar) in a linear scale, the signal on the x-axis is normalized *ext@peak*. The isotherms were measured at $20\,°C$ in a mixture of Ar and H_2. Note how the hysteresis (gap between absorption/desorption curves) decreases with increasing temperature. **Last figure:** Hysteresis of the pressure plateau is plotted versus annealing temperature. The hysteresis is calculated by interpolating the curves and taking the average of the hysteresis at 0.4, 0.5 and 0.6.

4.4.2 Varying Gold Concentration

As "500 °C, 2 h" seemed to be sufficient to form the alloy, this was chosen as the annealing scheme for the remainder of the project. This was used in order to investigate further aspects of the PdAu mixture. A few batches of particles with varying gold concentration and dimensions were fabricated in order analyse the influence of the gold concentration. A problem was found at higher concentrations, the particles seemed to not have relaxed before the isotherm measurements were done (making the isotherms irreversible) despite running 10 absorption cycles before measuring. A drift was detected in the LSPR signals, inducing an offset between the absorption/desorption curves. Another problem was to fit the LSPR peaks of all different particles within the analysis range of the instruments. When dimensions h,D were found with suitable LSPR peaks, particles of identical shape but varying gold concentration were fabricated.

In order to minimize the drift due to relaxation of the particles, approximately 60 hydrogenation cycles were performed (instead of the usual 5 as explained in figure 3.5). Hydrogen isotherms were then measured as before, see the result in figure 4.9. Note how the hysteresis decreases up to around 20 % Au. The signal contains considerable noise as well as drift for some samples (especially the 29 % sample), making a quantitative comparison of the hysteresis hard for these data. Instead the signal magnitude has been analysed, the last plot of the figure shows how the total centroid shift decreases somewhat with increasing gold concentration.

As these particles had the same shape (assuming that they deformed equally during annealing) they only differ in the composition. They were thus suitable for investigating the influence of the gold on the LSPR spectrum and were thus used inside the Cary spectrophotometer. In appendix A, a comparison of the spectra can be seen.
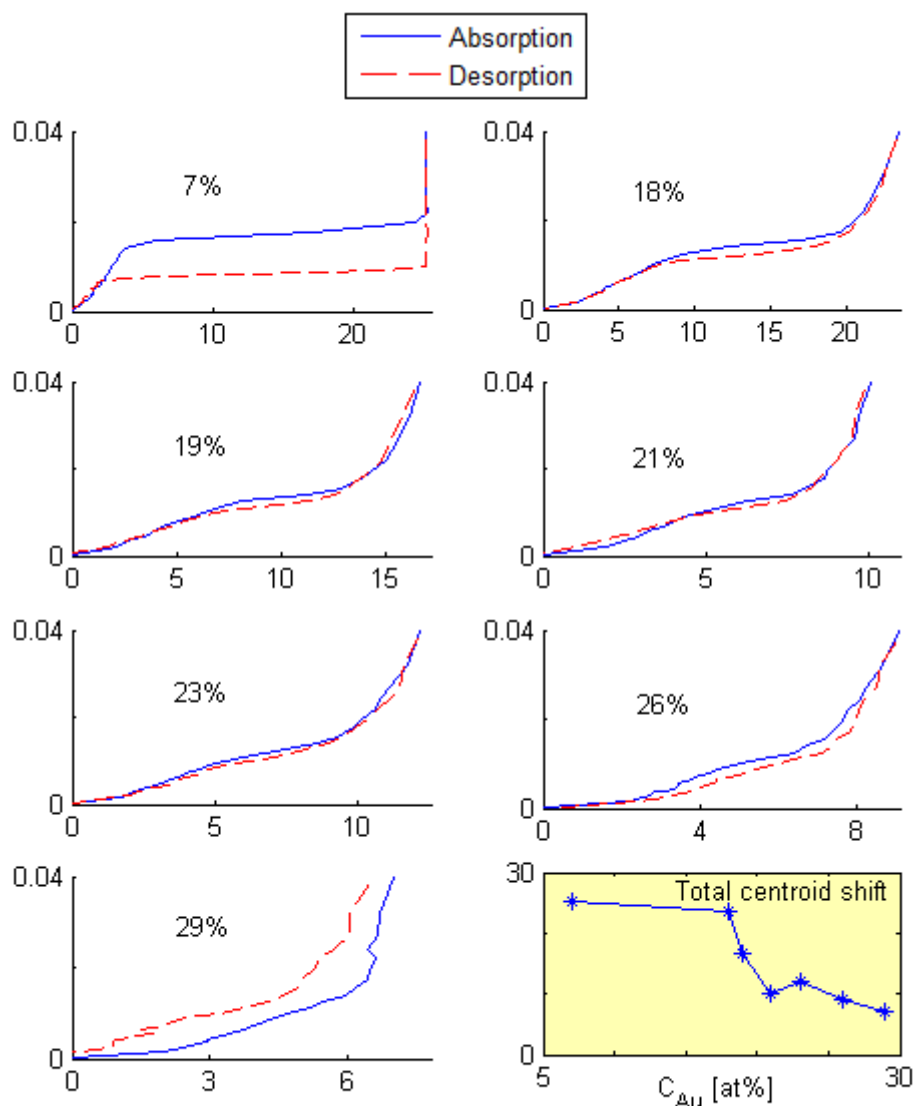
Figure 4.9: Figures 1-7: Hydrogen absorption/desorption isotherms for particles with varying gold concentration. Particles with $D \approx 190\,\text{nm}, h \approx 25\,\text{nm}$ were annealed during 2 hours at $500\,^\circ\text{C}$. The y-axis shows the hydrogen content of the gas mixture (i.e. the hydrogen pressure in bar), the signal on the x-axis is the centroid shift. Measured at $25\,^\circ\text{C}$ in a mixture of Ar and H_2. Note how the hysteresis between ab-/desorption becomes negligible compared to the noise above $\approx 20\,\text{at}\%$ but that a narrow hysteresis comes at the cost of a weaker signal. **Last figure:** Total signal (centroid shift [nm]) plotted versus gold concentration.

4.4.3 Kinetics

The kinetics of the hydrogen uptake can tell a lot about the system and in what way the gold affects the interaction between the hydrogen and the metal. It is also of certain interest when considering a sensor, possible users place high demands on fast response. The response time (absorption) and recovery time (desorption) were measured in the vacuum cell explained in section 3.2.2.

All samples that were measured had been annealed in $500\,^{\circ}C$ during $2\,h$. Prior to the kinetics measurement they had been exposed to up to 4% hydrogen during isotherm measurements in the X1 reactor. In order to stabilise the particles, every sample was exposed to at least 10 cycles of hydrogen/vacuum before any data was collected. The pressure during these cycles was held within $0.2-1\,bar$. This is a seemingly wide range but far above the pressure plateau at which the majority of the ab-/desorption takes place.
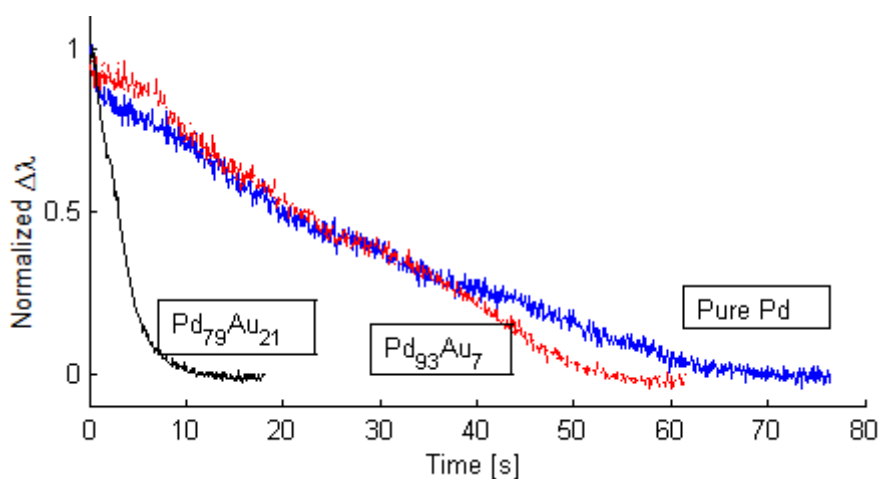
Figure 4.10: Hydrogen desorption curves for PdAu particles exposed to vacuum at $t = 0$. The signal on the y-axis is the normalized LSPR peak position.

In figure 4.10 three examples of desorption curves are given. Note the much longer time constant for the particles of low gold content as well as the shape of the curves. The slower curves seem have more linear shapes.

From this type of curve the recovery time could be obtained. It was defined as the time between the points where 10% and 90% of the signal change was reached (i.e. between the points $y = 0.9$ and $y = 0.1$ in figure 4.10). The same was done for absorption of hydrogen (going from vacuum to hydrogen gas). The result for both response and recovery time of different gold concentrations is presented in figure 4.11.

Note in the figure that the samples of very low Au concentration have considerably slower response. Note also that the response time is much faster than the recovery time, typically below 1 second. However, both curves seem to follow the same trend, increasing or decreasing between the same samples. This similarity between the trends is also seen

in a measurement of another batch of samples, see appendix B.
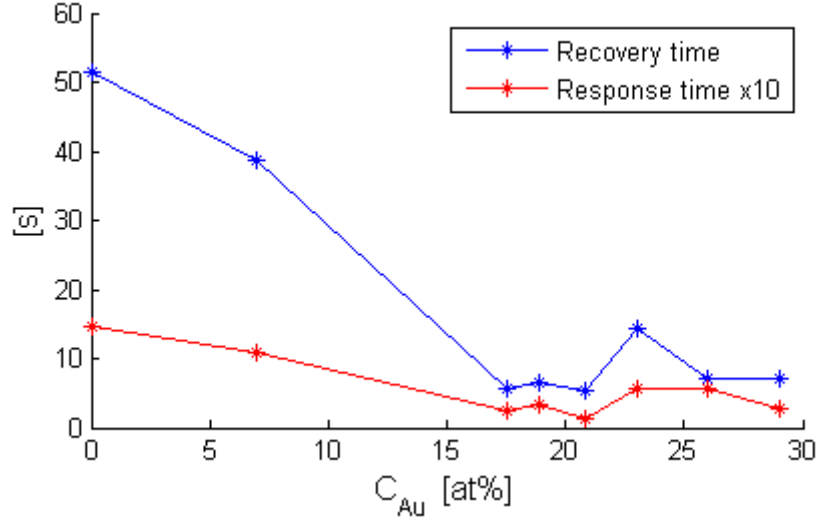
Figure 4.11: Response (absorption) and recovery (desorption) times for particles of varying Au concentration. The times have been measured as the time it takes to go from 10% to 90% signal shift of the LSPR peak position. The ab-/desorption was induced by changing the environment of the sample between vacuum and hydrogen gas at $P \approx 0.6$ bar. Note that the response time has been "magnified" an order of magnitude to make the shape of the curve clearer. Particle dimensions are $D \approx 190$ nm, $h \approx 25$ nm, and they have all been annealed in 500 °C during 2h.

5

Discussion

5.1 Alloy Formation

The main question of this thesis was whether an alloy could be fabricated with the limited methods at hand, i.e. annealing of two single metal layers. The experiments can also be seen as an assessment of the X1 reactor and the corresponding LSPR setup, evaluating its ability to induce and monitor alloying. Early in the project, it was believed that the alloying/mixing of the metals was the main reason of the LSPR peak shift upon annealing (seen in figure 4.1). However, in figure 4.2 a similar result is seen for pure Pd particles. The LSPR peak shift can thus not be used as an indicator of annealing on its own. The shift is most likely seen due to a geometry change, in the SEM analysis we can indeed see that the particles shrink when annealed (e.g figure 4.5).

The verification of alloy formation was instead provided by the XPS analysis. Samples annealed at $500\,^{\circ}\text{C}$ show a Pd-Au ratio at the surface that is very close to what was deposited. The annealing is further verified by the fact that the hydrogenation isotherms change upon annealing according to the hypothesis (the hysteresis is substantially more narrow). These results together form strong evidence of alloy formation, although complete homogeneity cannot yet be guaranteed.

5.1.1 Relevance for Other Alloys

The PdAu alloy nanoparticles might find their own applications in hydrogen sensing. It is also an interesting model system for other alloys, metal hydrides for energy storage being one example. This thesis presents a fabrication scheme that seems to produce alloyed PdAu particles, it is likely that the same method is applicable to other metal combinations as well. Whether annealing will work for a certain combination of metals will depend on the relation between the binding energies of those specific metals.

Although the peak position could not be used as indicator of alloying in this case, it might still prove useful in an early stage of development by giving hints about the

atomic mobility at different temperatures.

5.2 Properties of Alloy

5.2.1 Isotherms & Hysteresis

The results support the main hypothesis, the hysteresis indeed decreases when adding gold to the particles. The hysteresis seems to decrease with increasing gold content up to at least ≈ 20 at%. It is likely that further decrease could be detected above 20 at% if measuring with enough precision. The optimal hysteresis seems to be reached at 500 °C, although little data has been gathered for higher temperatures. Note also that apart from a decreasing hysteresis, an increased slope at the pressure plateau can be seen for higher concentrations of gold (see figure 4.9).

A similar decrease in hysteresis for PdAu thin films is seen by *Westerwaal et al.* [21]. However, their isotherms differ in some ways. The main difference is the signal strength decrease. The signal measured on the thin films(reflectivity) is about 4 times lower for 18.9 at% gold than for 8.6 at%, while the total centroid shift of our nanoparticles (see figure 4.9) barely decreases between 7 at% and 18 at%.

Westerwaal et al. partly attribute the lack of hysteresis to a lowering of T_c, the temperature at which an ideal metal-hydride system "loses" the pressure plateau. However, the isotherms of figure 4.9 seem to exhibit a pressure plateau, although the hysteresis is nearly gone.

An interesting similarity can also be found when looking at hydrogen uptake in small Pd particles. The hysteresis disappears and the slope of the pressure plateau increases when decreasing the size of pure Pd particles (seen for particles of $D < 10$ nm)[40] in the same way as when increasing the gold content of larger particles. In the case of the small particles the features are attributed to higher influence of lattice strain and surface tension. Perhaps this attribution is also reasonable in the case of PdAu particles. The addition of gold might decrease the energy gain of the hydrogen occupying the interstitial sites, making the lattice strain relatively stronger. One can also imagine that the presence of gold makes some interstitial sites completely energetically unfavourable, interrupting the network of hydrogen particles in the β-phase and decreasing the energetic gain provided by the attractive H-H interaction.

5.2.2 Kinetics

The kinetics measured in the vacuum cell (see figure 4.11) point to another possible advantage of adding gold to the particles, faster response/recovery times compared to pure Pd. Other factors may have influenced the results (perhaps the "slowest" particles were just more contaminated) but the time scale of the pure Pd sample agrees with earlier results for Pd particles measured at $T = 30°$ [40]. Thus it seems that the decreased response/recovery time can truly be attributed to the increase of gold concentration.

The trend is not a monotonous down-slope, there are also variations among the

gold-rich samples. These differences may indeed be due to other effects, such as contamination, and few conclusions can therefore be drawn.

However, the differences are still of interest and worth noting as almost the same variations are seen for the recovery time as for the response time (also see appendix B for further examples of this). This might seem completely reasonable but absorption and desorption in pure palladium are limited by different phenomena. The absorption rate is limited by diffusion through the metal while the desorption rate is limited by H-H association at the Pd surface[40]. The gold content (or something else) seems to affect both these rate limiting steps in the same way. Another explanation might be that, in the case of PdAu, the diffusion is so much faster that both rates are limited by effects at the surface. Why is then the diffusion so much faster? Speculatively, it could be explained by the gold making the interstitial lattice sites less energetically favourable for the hydrogen, decreasing the energy barrier for moving between sites.

5.2.3 Producing a Sensor?

When discussing the suitability of the PdAu alloy as a sensing material it is interesting to look back at the background, particularly tables 2.1 and 2.2. The measuring range of "up to 4vol%" is fulfilled. The detection limit for the automobile applications (0.1 vol%) is likely fulfilled as the slope of the $P - \Delta\lambda$ curves is fairly "flat" at low H_2 pressures(i.e. low concentrations) and thus have a high resolution. The requirement of stationary systems (100 ppm) is tougher but might be possible if the noise can be minimised. The response/recovery times (30/60 seconds) of the stationary system is fulfilled for all studied PdAu samples. The automobile sector puts higher demands on these rates and a recovery time of 1 s is probably very hard to achieve. Perhaps it would be possible to achieve by making the particles smaller and optimise the particle surface for functionality.

The accuracy requirement of the stationary systems, ±25 %, is likely possible to meet. The requirement ±5 % of the car industry is harder to fulfil. The hysteresis and/or noise of the particles seems to be of greater magnitude than 5 % in most isotherms of figure 4.9. The hysteresis might be low enough above a certain percentage of gold but this would also decrease the signal strength.

The signal-to-noise ratio of a sensor would depend on many factors. Material properties, such as gold content, influence the signal strength. The gold content also affects the slope of the $P - \Delta\lambda$ curve, determining how much error in the pressure reading that the noise corresponds to. This increase in slope is attributed to the gold introducing a distribution in the energy of the interstitial sites according to *Westerwaal et al.* [21]. Perhaps this energy-distribution can be optimised depending on where in the pressure range the flattest slope is desired. For example one might achieve this by tuning the gold concentration, using different gold concentrations in different particles or combine more metals.

The signal-to-noise ratio is also highly dependent on the LSPR sensing setup. The light source, optics and the sensor need to be optimised depending on the application and its requirements on accuracy, size and cost. For some applications, e.g. mass

produced vehicles, it may not be economically viable to use a spectrophotometer and the signal would then, in some aspects, behave differently from what has been presented in this thesis. A cheap solution could be to use a laser and measure the extinction at the single wavelength of the laser. However, it would be beneficial to utilise the wavelength-dependency of the nanoparticles as this decreases the uncertainties due to intensity fluctuations (i.e. dust or light source aging). Perhaps a compromise is to measure the ratio between two wavelengths or in another way compare the intensity of a small number of wavelengths. Light source fluctuations can also be dealt with by using the same light source to monitor a "blank" sample, without particles that interact with the hydrogen.

So, how accurate could our sensor be in the ideal case? According to earlier studies, it is possible to achieve a $0.01\,nm$ precision in the centroid measurement[33]. What precision in the hydrogen concentration does this correspond to? Let us look at the last part of the $19\,at\%$-Au sample of figure 4.9 as an example. In this part the curve has a slope of $1\,\%/nm$ which would correspond to a precision of $0.01\,\%H_2$ with an ideal centroid measurement.

5.3 Experimental Uncertainties

The most important uncertainty in the data of this thesis is the gold content of the particles. In section 3.1.2 we discussed the metal deposition and concluded that an uncertainty of typically $\approx 1-2$ percentage points exists due to the time it takes to open/close the shutter. The Pd-Au ratio that has been presented is the atomic ratio that corresponds to the thickness that was specified to the evaporator when depositing each layer. This was chosen throughout this thesis for consistency. It is not in perfect accordance with the real particles due to the uncertainty mentioned above and also due to the fact that the holes of the mask shrink as material is deposited. Due to this shrinking, the particles are shaped like truncated cones rather than cylinders, something that has not been accounted for when specifying the composition. This should be taken into account by anyone that uses this work in order to, for example, chose a suitable composition in the beginning of their own project.

Another fabrication uncertainty is the exact annealing temperature. The temperature measured by the thermocouples may not be representable for the whole sample.

In the case of the isotherm measurements in the X1 reactor the main uncertainties are noise and drift in the LSPR signals(e.g. $29\,at\%$ of figure 4.9). The drift seen in some measurements may be due either to changes in the particles(gold migration, relaxation of the lattice et cetera.) and/or light source fluctuations. Fluctuations in the light source intensity have been detected during some measurements. If such a fluctuation is due to variations in the temperature of the light source, fluctuations in the spectrum are also probable (which in turn would affect the centroid).

5.4 Outlook

Although the results are pointing to alloying and homogeneity after annealing at 500 °C, further research on the annealing and the resulting particle composition would indeed be interesting. For example, there could potentially be small regions, such as the surface or grain boundaries, that are richer in gold or palladium. It is possible that the annealing could be further optimised, perhaps by increasing the cooling rate or by decreasing the concentration of oxygen and other contamination in the chamber. This thesis has mainly discussed gold and palladium, other materials might prove superior over gold for different reasons.

Optimising the setup and the material for accuracy is interesting in several aspects. As an engineer it is crucial in order to produce a sensor. As a scientist, this is interesting in order to further understand the hydrogen uptake characteristics. With less noise, one can analyse if (and how) the hysteresis decreases further with gold concentrations above $\approx 20 \, \mathrm{at\%}$.

The kinetic measurements were done last of all but might have raised the most interesting questions. Why is the absorption/desorption so much faster for gold-rich particles? How have the rate limiting steps changed? The kinetics could be further analysed by measuring at different temperatures and perhaps while varying other parameters such as the particle size and surface area.

6

Conclusions

PdAu nanoparticles were fabricated by annealing of two single metal layers. Alloying was confirmed for annealed samples, complete intermixing is believed to happen for samples annealed at $\approx 500\,°C$ during 2 hours. XPS measurements have shown that the gold has migrated through the palladium and that the particles are nearly homogeneous. SEM analysis has shown that the particle diameter has decreased somewhat.

The alloying is also confirmed by the hydrogen uptake properties of the particles. In agreement with the hypothesis, the hysteresis of the ab-/desorption isotherms decreased with increasing gold concentration and nearly vanished for samples of $20\,at\%$ or more. The isotherms of gold-rich alloys also show a decrease in signal (LSPR centroid shift) and an increasing slope of the pressure plateau. The result is similar to that of thin films although (at least if considering the LSPR centroid) the signal strength does not decrease as much for the nanoparticles as for the film. Some drift has been observed in the LSPR signals, the origin so far uncertain.

The addition of gold speeds up the kinetics of hydrogen absorption/desorption and might change the rate limiting step of the absorption.

PdAu alloy nanoparticles may in many aspects improve the sensing characteristics of optical hydrogen sensors that today implement thin Pd-films. It may be particularly advantageous in applications that need a high accuracy reading in the range where the hysteresis normally introduces uncertainty. More research is of course needed, especially in order to assess the long-term stability of the alloy.

Bibliography

[1] Carl Wadell 2012 *Nanoplasmonics for Absorption Engineering and Hydrogen Sensing* Licentiate Thesis, Chalmers University of Technology, Göteborg, Sweden

[2] Louis Schlapbach & Andreas Züttel 2001 *Hydrogen-storage materials for mobile applications* Nature VOL 414 353-358

[3] Joshi A.S. , Dincer I. , Reddy B.V. 2011 *Solar hydrogen production: A comparative performance assessment* International Journal of Hydrogen Energy Volume 36, Issue 17 11246-11257

[4] Amjad Riaz, Gholamreza Zahedi, Jirí Jaromír Klemes 2013 *A review of cleaner production methods for the manufacture of methanol* Journal of Cleaner Production 57, 19-37

[5] C. Bernaya, M. Marchanda, M. Cassir 2001 *Prospects of different fuel cell technologies for vehicle applications* Journal of Power Sources 108 (2002) 139–152

[6] I.P. Jain, Chhagan Lal, Ankur Jain 2010 *Hydrogen storage in Mg: A most promising material* International Journal of Hydrogen Energy Volume 35 (2010) 5133 – 5144

[7] Ki-Joon Jeon, Hoi Ri Moon2, Anne M. Ruminski, Bin Jiang, Christian Kisielowski, Rizia Bardhan and Jeffrey J. Urban 2011 *Air-stable magnesium nanocomposites provide rapid and high-capacity hydrogen storage without using heavy-metal catalysts* NATURE MATERIALS VOL 10 286-290

[8] `http://en.wikipedia.org/wiki/Honda_FCX_Clarity`

[9] `http://en.wikipedia.org/wiki/BMW_Hydrogen_7`

[10] Wikipedia user *Bbqjunkie*, found at `http://en.wikipedia.org/wiki/File:FCX_Clarity.jpg`

[11] US Department of Energy 2012 *Fuel Cell Technologies Office Multi-Year Research, Development and Demonstration Plan, 3.1 Hydrogen Storage* `http://www1.eere.energy.gov/hydrogenandfuelcells/mypp/`

[12] Suzuki, J., Tamura Y., Watanabe S., Takabayashi M., Sato K. 2006 *Fire safety evaluation of a vehicle equipped with hydrogen fuel cylinders: Comparison with gasoline and CNG vehicles* 2006 SAE World Congress; Detroit, MI; United States

[13] Suman Dutta 2006 *A review on production, storage of hydrogen and its utilization as an energy resource* Journal of Industrial and Engineering Chemistry, Available online 2 August 2013, ISSN 1226-086X

[14] A. Montone, A. Aurora, D. Mirabile Gattia and M. Vittori Antisari 2010 *On the barriers limiting the reaction kinetics between catalysed Mg and hydrogen* Scripta Materialia 63 456–459

[15] E. Callini, L. Pasquini, T.R. Jensen, E. Bonetti 2013 *Hydrogen storage properties of Mg-Ni nanoparticles* International journal of Hydrogen Energy 38 12207-12212

[16] G. Liang, S. Boily, J. Huot, A. Van Neste, R. Schulz 1998 *Mechanical alloying and hydrogen absorption properties of the Mg–Ni system* Journal of Alloys and Compounds 267 302–306

[17] Chang Yang, Lun Ma, Xiaoju Zou, Guangya Xiang, Wei Chen 2013 *Surface plasmon-enhanced Ag/CuS nanocomposites for cancer treatment* Cancer Nanotechnology Volume 4, Issue 4-5, pp 81-89

[18] Christoph Langhammer 2009 *Nanoparticle Plasmons in Classic and Novel Material - Fundamentals and Hydrogen Sensing* Doctoral dissertation, Chalmers University of Technology, Göteborg, Sweden

[19] Nirag Kadakia, Mengbing Huang, Hassaram Bakhru 2011 *Embedded silver nanoparticle fabrication for surface plasmon-enhanced silicon photovoltaics* Conference: Next Generation (Nano) Photonic and Cell Technologies for Solar Energy Conversion II Loucas Tsakalakos San Diego, California | August 21, 2011

[20] nanoComposix 2012 `http://nanocomposix.com/technology/plasmonics-and-nanophotonics`

[21] R.J. Westerwaal, J.S.A. Rooijmans, L. Leclercq, D.G. Gheorghe, T. Radeva, L. Mooij, T. Mak, L. Polak, M. Slaman, B. Dam, Th. Rasing 2013 *Nanostructured Pd-Au based fiber optic sensors for probing hydrogen concentrations in gas mixtures* International journal of Hydrogen Energy 38 4201-4212

[22] L. Boon-Brett, J. Bousek, G. Black, P. Moretto, P. Castello, T. Hübert b, U. Banach 2010 *Identifying performance gaps in hydrogen safety sensor technology for automotive and stationary applications* International journal of Hydrogen Energy 35 373-384

[23] Cedric Perrotton, Nicolas Javahiraly, Alex Kazemi and Patrick Meyrueis 2011 *Review of optical fiber sensor technologies for hydrogen leak detection in hydrogen*

energy storage From Conference Volume 8026 Photonic Applications for Aerospace, Transportation, and Harsh Environment II, Orlando, Florida, USA

[24] http://en.wikipedia.org/wiki/Palladium#cite_note-unctad-32

[25] Raymond E. Schaak, Amandeep K. Sra, Brian M. Leonard, Robert E. Cable, John C. Bauer, Yi-Fan Han, Joel Means, Winfried Teizer, Yolanda Vasquez, and Edward S. Funck 2005 *Metallurgy in a Beaker: Nanoparticle Toolkit for the Rapid Low-Temperature Solution Synthesis of Functional Multimetallic Solid-State Materials* J. Am. Chem. Soc. 127(10)

[26] Riccardo Ferrando, Julius Jellinek, and Roy L. Johnston 2008 *Nanoalloys: From Theory to Applications of Alloy Clusters and Nanoparticles* Chemical Reviews Volume 108, Number 3

[27] David Monzón-Hernández, Donato Luna-Moreno, Dalia Martínez-Escobar 2009 *Fast response fiber optic hydrogen sensor based on palladium and gold nano-layers* Sensors and Actuators B 136 (2009) 562–566

[28] Cédric Perrotton, Ruud. J. Westerwaal, Nicolas Javahiraly, Martin Slaman, Herman Schreuders, Bernard Dam, and Patrick Meyrueis 2013 *A reliable, sensitive and fast optical fiber hydrogen sensor based on surface plasmon resonance* Optics Express, Vol. 21, Issue 1, pp. 382-390

[29] Christoph Langhammer, Bengt Kasemo and Igor Zoric 2007 *Absorption and scattering of light by Pt,Pd,Ag, and Au nanodisks: Absolute cross sections and branching ratios* THE JOURNAL OF CHEMICAL PHYSICS 126, 194702

[30] A. Li, W. Liang, R. Hughes 2000 *The effect of carbon monoxide and steam on the hydrogen permeability of a Pd/stainless steel membrane* Journal of Membrane Science 165 135–141

[31] Z. Zhao & M.A. Carpenter 2005 *Annealing enhanced hydrogen absorption in nanocrystalline Pd/Au sensing films* J. Appl. Phys. 97 124301

[32] Fredriksson, H.; Alaverdyan, Y.; Dmitriev, A.; Langhammer, C.; Sutherland, D.; Zäch, M.; Kasemo, B. 2007 *Hole-Mask Colloidal Lithography* Advanced Materials 19, 4297-4302

[33] Andreas B. Dahlin, Jonas O. Tegenfeldt, and Fredrik Höök 2006 *Improving the Instrumental Resolution of Sensors Based on Localized Surface Plasmon Resonance* Analytical Chemistry 78, 4416-4423

[34] Nicholas J. Goddard, Denise Pollard-Knight and Colin H. Maule 1994 *Real-time Biomolecular Interaction Analysis Using the Resonant Mirror Sensor* Analyst, Vol. 119, pp 583-588

[35] http://en.wikipedia.org/wiki/Scanning_electron_microscope

[36] Carl Zeiss AG, *SUPRA VP Technical Data*, Found at `http://www.zeiss.com/` `C1256E4600307C70/EmbedTitelIntern/SUPRA_VP_TechnicalData/\protect\` `T1\textdollarFile/SUPRA_VP_Technical_Data.pdf` 2013-11-20

[37] `http://rsb.info.nih.gov/ij/`

[38] `http://en.wikipedia.org/wiki/X-ray_photoelectron_spectroscopy`

[39] Moulder J.F., Stickle W.F., Sobol P.E. and Bomben K.D. 1992 *Handbook of X-ray Photoelectron Spectroscopy* Eden Prairie, Minnesota, United States of America, Perkin-Elmer Corporation

[40] Christoph Langhammer, Elin M. Larsson, Bengt Kasemo, and Igor Zoric 2010 *Indirect Nanoplasmonic Sensing: Ultrasensitive Experimental Platform for Nanomaterials Science and Optical Nanocalorimetry* Nano Letters 2010, 10, 3529–3538

A

Spectra

The extinction spectra for some samples were measured in the *Cary* spectrophotometer, see figure A.1.
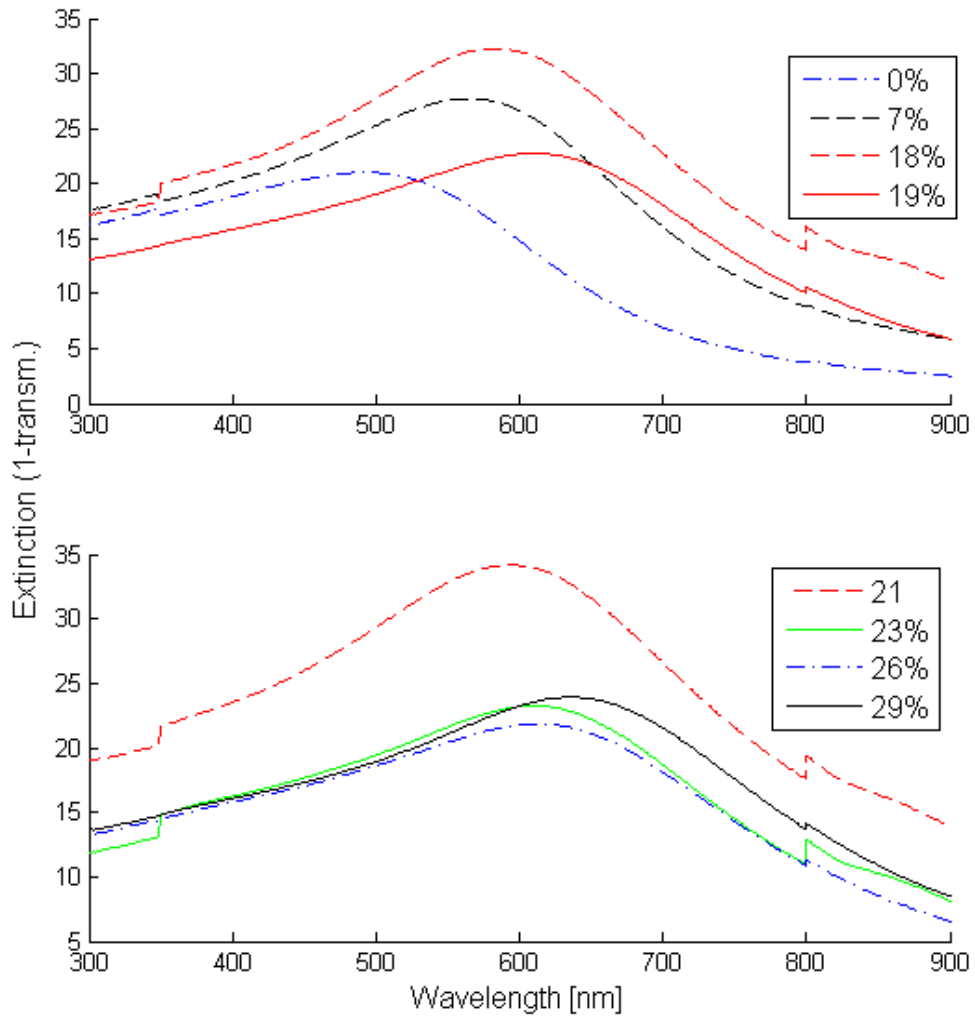
Figure A.1: The extinction spectra of particles with varying gold concentration. The particles were fabricated with the dimensions $D = 25\,\text{nm}$, $h = 190\,\text{nm}$ and were then annealed at $500\,°\text{C}$ during 2h.

B

Additional Kinetics

In order to further demonstrate the similarity between the trends of the response- and recovery time, I here present additional data in figure B.1. Note that the samples have all been prepared in somewhat different ways, no conclusions apart from the "trend similarity" should thus be taken from the figure.
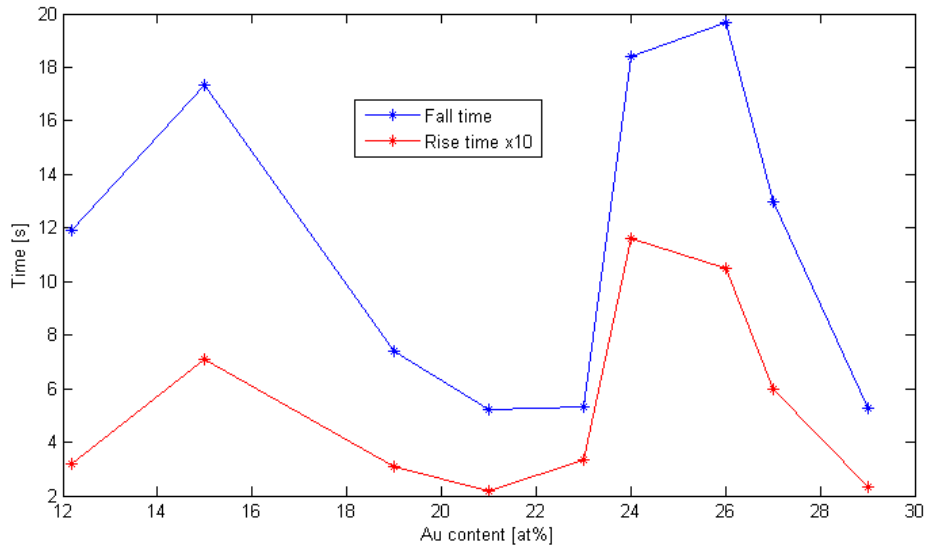
Figure B.1: Response (absorption) and recovery (desorption) times for particles of varying Au concentration. The particles also varied in other ways, they were of different size and some had been cleaned in an oxygen plasma etch. The times have been measured as the time it takes to go from 10% to 90% signal shift of the LSPR peak position. The ab-/desorption was induced by changing the environment of the sample between vacuum and hydrogen gas at $P \approx 0.6$ bar. Note that the response time has been "magnified" an order of magnitude to make the shape of the curve clearer.